Footprints of Lagrangian flow structures in Eulerian transport

M.F.M. Speetjens,[1] M. Lauret, H. Nijmeijer, P.D. Anderson
Eindhoven University of Technology, Department of Mechanical Engineering
PO Box 513, 5600 MB Eindhoven, The Netherlands

Abstract

Transport of passive tracers may be described through the spatio-temporal evolution of Eulerian tracer distributions or via the geometrical composition of the Lagrangian flow structure. The present study seeks to deepen insight into the connection between the Eulerian and Lagrangian perspectives by investigating the role of Lagrangian coherent structures (LCSs) in the Eulerian tracer distributions. Representation of the Eulerian transport by the mapping method, describing realistic transport problems by distribution matrices, admits a generic analysis based on matrix and graph theory. This reveals that LCSs – and the transport barriers that separate them – leave a distinct "footprint" in the eigenmode spectrum of the distribution matrix and, by proxy, of the underlying Eulerian transport operator. The composition of the distribution matrix versus the Lagrangian flow structure thus predicted is demonstrated by way of examples. These findings increase fundamental understanding of transport phenomena and have great practical potential for e.g. flow and mixing control.

1. Introduction

Understanding the relation between flow and effective mixing of scalars (chemical species, heat, nutrients) is important for many processes in industry and Nature [1–5]. Accomplishment of efficient mixing in low-Reynolds num-

[1]Corresponding author: m.f.m.speetjens@tue.nl

ber flows by way of chaotic advection has been a research topic since the early 1980s [6–8] and attracted renewed interest over the last decade or so with the emergence of compact and micro-scale fluid-processing devices for a wide range of applications [9–16]. Great fundamental insight into the workings of chaotic advection has been attained by analysis of the advection of passive tracers ("distributive mixing")[2] adopting Lagrangian concepts from dynamical-systems theory (critical points, transport barriers, manifolds *etc*) [4, 7, 8, 17]. Key to this ansatz is the fundamental property that continuity organizes the trajectories of passive tracers into coherent structures – termed "Lagrangian coherent structures" (LCSs) hereafter – that geometrically determine the advection characteristics.[3] The set of finest LCSs that constitute the Lagrangian flow structure is the so-called ergodic partition [19, 20]. Well-known examples of LCSs are elliptic islands and chaotic seas in two-dimensional (2D) time-periodic flows and cross-sections of three-dimensional (3D) steady spatially-periodic flows. The present study is restricted to these important flow classes.

An alternative approach towards transport and mixing consists of an Eulerian representation based on the spatio-temporal evolution of the scalar field, which is determined by the eigenmodes of the transport operator. Eigenmode analyses on transport operators have to date been performed primarily in the scope of advective-diffusive scalar transport and advanced insightful concepts as dominant (or "strange") eigenmodes that govern the scalar evolution [21–23]. An important issue is the role of (chaotic) advection in the spectral properties of the advection-diffusion operator. Insight into this connection is imperative for control strategies employing the flow forcing, which is typically the only degree

[2]Diffusive and distributive mixing refer to scalar transport with and without diffusion, respectively, within the scope of this study. This is common yet not exclusive terminology. Absence of diffusion means that an initial state is merely redistributed by the fluid motion while initial quantities are conserved by each fluid parcel. Fluid parcels thus carrying a scalar quantity are denoted "passive tracers" here.

[3]Important to note is that the term "Lagrangian coherent structures" (LCSs) in the present context refers to invariant material structures in the fluid trajectories; LCSs in literature typically denote surfaces that are demarcated on the basis of (finite-time) Lyapunov exponents. The relation between both kinds of LCSs is non-trivial and remains unsettled [18].

of freedom in a given system, for regulation of the transport process. This has particular potential for micro-fluidic applications, where promising flow-forcing methods as e.g. artificial cilia, magnetic forcing and AC electro-osmosis afford many ways to manipulate the flow [24–27]. Better control of flows and associated LCSs may, besides mixing enhancement, enable systematic creation of distinct concentration distributions or Lagrangian flow structures for e.g. (local) catalysation of chemical reactions in labs-on-a-chip or manufacturing of anisotropic micro-fibres.

In its advective limit, the eigenmodes of the advection-diffusion operator are intimately related to the Lagrangian flow structure [28, 29]. This implies that LCSs, at least in said limit, leave distinct footprints in the Eulerian transport by determining the eigenmodes of the transport operator [19, 20]. Scope of the current investigation is formation of such footprints in the aforementioned classes of periodic flows. To this end the advection operator is represented by a distribution matrix according to the mapping method so as to attain a universal description that is amenable to efficient numerical treatment [30–33]. This facilitates rigorous analyses using graph and matrix theory and, with flow control a potential application of knowledge gathered, already sets the stage for future links with control theory. Singh *et al.* [34] first embarked on this course and exposed a number of fundamental connections between the eigenmode decomposition of the mapping matrix and LCSs. The present study expands on this by further unravelling the connections between Eulerian and Lagrangian transport properties using the mapping method.

The paper is organized as follows. Section 2 introduces the mapping method for distributive mixing and recapitulates first connections between its distribution matrix and LCSs found in previous work. Section 3 expands on this by establishing a rigorous link between the composition of said matrix and two key LCSs, viz. elliptic islands and chaotic seas, by way of an in-depth analysis hinging on graph and matrix theory. The impact of numerical effects on this link is investigated in Section 4. Conclusions are in Section 6.

2. Distributive mixing in periodic flows

2.1. Introduction

The present study concerns 2D time-periodic flows and 3D steady spatially-periodic flows. Both flow types essentially have the same structure and admit a representation by 2D time-periodic flows without loss of generality [34]. Advective-diffusive transport of a passive scalar quantity $c(\boldsymbol{x},t)$ by a time-periodic flow $\boldsymbol{u}(\boldsymbol{x},t)=\boldsymbol{u}(\boldsymbol{x},t+T)$, with period time T and subject to solenoidality $\nabla\cdot\boldsymbol{u}=0$, in the generic 2D domain $\mathcal{D}$ is governed by

$$\frac{\partial c}{\partial t}=-\boldsymbol{u}\cdot\nabla c+\frac{1}{\mathrm{Pe}}\nabla^2 c,\qquad c(\boldsymbol{x},0)=c_0(\boldsymbol{x}), \tag{1}$$

completed by boundary conditions defined on boundary $\partial\mathcal{D}$. Here $\mathrm{Pe}=UL/\kappa$ is the Péclet number, with U and L the characteristic velocity and length scale respectively and where κ is the mass-diffusion coefficient [35]. Distributive mixing (i.e. advective transport by fluid motion only) occurs in case diffusion is absent and corresponds with the limit $\mathrm{Pe}\to\infty$.

Periodic scalar transport can be described by the Floquet operator $\mathcal{F}$, which maps the scalar distribution between discrete time levels $t=nT$, where $n\in\mathbb{N}$ a positive integer, via

$$c(\boldsymbol{x},T)=\mathcal{F}\left(c(\boldsymbol{x},0)\right),\qquad c(\boldsymbol{x},(n+1)T)=\mathcal{F}\left(c(\boldsymbol{x},nT)\right),\qquad c(\boldsymbol{x},nT)=\mathcal{F}^n\left(c_0(\boldsymbol{x})\right) \tag{2}$$

and thus incorporates the integral effect of the advection-diffusion operator within one period.[4] The Floquet operator permits the eigenmode decomposition

$$c(\boldsymbol{x},nT)=\sum_{k=0}^{\infty}\gamma_k\mathcal{H}_k^{(n)}(\boldsymbol{x}),\qquad \mathcal{H}_k^{(n)}(\boldsymbol{x})=\nu_k^n\Theta_k(\boldsymbol{x}), \tag{3}$$

with $\mathcal{H}_k^{(n)}$ the eigenmodes and $\{\Theta_k,\nu_k\}$ the corresponding eigenfunction-eigenvalue pairs governed by the eigenvalue problem $\mathcal{F}(\Theta_k)-\nu_k\Theta_k=0$ and coefficients γ_k determined by the initial state [34, 36]. For distributive mixing ($\mathrm{Pe}\to\infty$)

[4] Term "Floquet operator" refers specifically to time-periodic systems; the transport operator is for generic time-dependence commonly denoted "Frobenius-Perron operator" [23].

the scalar c becomes a passive tracer (i.e. a "label" for fluid parcels due to $\partial c/\partial t + \boldsymbol{u} \cdot \boldsymbol{\nabla} c = dc/dt = 0$) and the Floquet operator in essence describes the period-wise mapping of tracer positions following

$$\mathcal{F} : \boldsymbol{x}_n \to \boldsymbol{x}_{n+1}, \qquad \boldsymbol{x}_n = \boldsymbol{x}(nT), \tag{4}$$

and thus effectively coincides with the flow $\boldsymbol{x}_{n+1} = \boldsymbol{F}(\boldsymbol{x}_n)$ governed by the Lagrangian equations of motion $d\boldsymbol{x}/dt = \boldsymbol{u}$. (The Floquet operator in fact identifies with the Koopman operator in this limit [28].) This has the fundamental ramification that in the limit $\mathrm{Pe} \to \infty$ the scalar transport properties become inextricably linked with Lagrangian coherent structures (LCSs) that form in the web of fluid trajectories by virtue of continuity. Important to note is that the mapping representation of the transport operator introduced hereafter, though strictly concerning purely advective transport, introduces diffusion-like behavior to the dynamics that closely resembles molecular diffusion at very high Pe [37]. The present study demonstrates that this is inconsequential in the sense that the abovementioned link with LCSs remains sufficiently intact, however. Moreover, this slight diffusion, though of numerical origin, is in fact physically meaningful in the sense that at some length scale molecular diffusion invariably comes into play in a real flow.

An illustrative example of transport in 2D time-periodic flows is found in the time-periodic sine flow (TPSF) on the 2-torus $(x, y) \in [0, 1] \times [0, 1]$ [34, 36]. The TPSF consists of periodic reorientation of steady velocity fields: $\boldsymbol{u} = (\sin(2\pi y), 0)$ for $0 < t < T/2$ and $\boldsymbol{u} = (0, \sin(2\pi x))$ for $T/2 < t < T$. The TPSF admits an analytical solution to the Lagrangian equations of motion and thus enables highly-accurate visualisation of its Lagrangian flow structure by Poincaré sections. Figure 1 gives the latter for $T = 0.56, T = 0.8$ and $T = 1.6$, exposing the characteristic flow structure of 2D mixing flows: islands and chaotic seas. The progression with growing T reveals a gradual diminution of islands in favor of a chaotic sea until a state of global chaos sets in beyond a certain T.

Islands consist of concentric closed invariant curves, that is, the well-known KAM tori [7, 38]. They act as as transport barriers to scalar redistribution

and the outermost KAM torus of an island physically separates its interior from the surrounding chaotic sea. Perturbation typically causes disintegration of islands into smaller islands and encircling "island chains" embedded in chaotic "bands" following the KAM and Poincaré-Birkhoff theorems [7, 38]. However, the outermost KAM torus of each island remains a strict transport barrier. KAM tori on the brink of disintegration typically develop leaks, a state referred to as "cantorus," and thus form an intricate local Lagrangian flow structure that partially acts as a transport barrier and partially facilitates weak dispersion of material across the (originally complete) KAM torus [39, 40]. Islands and chaotic seas are two key features of the Lagrangian flow structure (or ergodic partition) of periodic flows and the primary subjects of investigation hereafter.

The organization into islands and seas in fact stems from periodic points, i.e. material points that systematically return to their initial position after a given number of periods p, defined by $\boldsymbol{x}^{(0)} = \boldsymbol{F}^p(\boldsymbol{x}^{(0)})$. Incompressible 2D time-periodic flows admit two non-degenerate types: elliptic and hyperbolic periodic points. Former and latter locally organize the tracer paths into islands and chaotic seas, respectively. LCSs within chaotic seas are the stable and unstable manifolds associated with each hyperbolic point; these manifolds accomplish the characteristic exponential stretching and folding of fluid parcels that underlies chaotic advection [7, 38]. Periodic points – and accompanying LCSs – may emerge isolated (periodicity $p = 1$) or in clusters (periodicity $p > 1$) of p points $\boldsymbol{\mathcal{X}} = \left\{\boldsymbol{x}^{(0)}, \boldsymbol{x}^{(1)}, \ldots, \boldsymbol{x}^{(m)}, \ldots, \boldsymbol{x}^{(p-1)}\right\}$, with $\boldsymbol{x}^{(0)} = \boldsymbol{F}^p(\boldsymbol{x}^{(0)})$ and $\boldsymbol{x}^{(n)} = \boldsymbol{F}^n(\boldsymbol{x}^{(0)})$ [41, 42]. Essential is that material wanders progressively through the consecutive elements yet clusters as a whole are invariant. Island chains e.g. encompass p islands that each are centered on one of the points belonging to a cluster of p elliptic period-p points; chaotic seas may originate from manifolds of clusters of higher-order periodic points. Here islands for $T = 0.56$ and $T = 0.8$ correspond with two isolated period-1 and two clusters of period-2 points, respectively. The pair-wise emergence is in both cases a manifestation of the time-reversal symmetry $\boldsymbol{F} = S\boldsymbol{F}^{-1}S$, with $S : (x, y) \to (y, 1 - x)$, by which LCSs $\mathcal{C}$ emerge in symmetry groups $(\mathcal{C}, S(\mathcal{C}))$ [42].

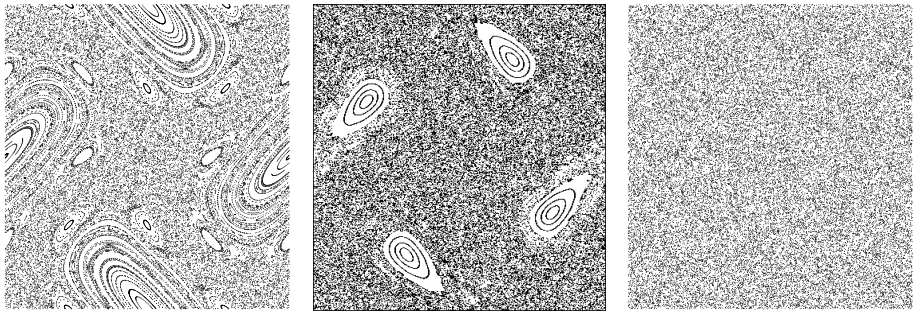

(a) (b) (c)

Figure 1: Typical 2D Lagrangian flow structure illustrated by way of the Poincaré section of the TPSF for various T: (a) $T = 0.56$; (b) $T = 0.8$; (c) $T = 1.6$.

Shown Lagrangian flow structure is intimately related to the eigenmodes $\mathcal{H}_k^{(n)}$ of the underlying transport operator [28, 29]. Hence, an eigenmode analyses of this operator is expected to provide fundamental insight into the transport properties of distributive mixing. An efficient and flexible way to carry out eigenmode analyses is by way of the mapping method, which enables a discrete approximation of the Floquet operator in a wide range of flow situations by so-called mapping matrices. The composition of these matrices, notwithstanding weak diffusion-like effects inherent in the discretisation, relates directly to the LCSs and thus reflects the link between Eulerian and Lagrangian transport properties of a given flow. First connections between this matrix composition and LCSs have been established in Singh *et al.* [34] The study hereafter further elaborates this.

2.2. Distributive mixing described by the cell-mapping method

The cell-mapping method, originally proposed by Spencer and Wiley [43], describes mixing within each period by the redistribution of scalar quantities $c(\boldsymbol{x}, t)$ over a discrete grid of N cells. This redistribution is area-preserving for solenoidal flow fields $\boldsymbol{\nabla} \cdot \boldsymbol{u} = 0$, meaning that in the present limit of distributive mixing a given amount of material is proportional to the area of the material fluid element it occupies. This renders the scalar redistribution equivalent to the redistribution of initial areas A_j of each cell Ω_j over all cells of the mapping

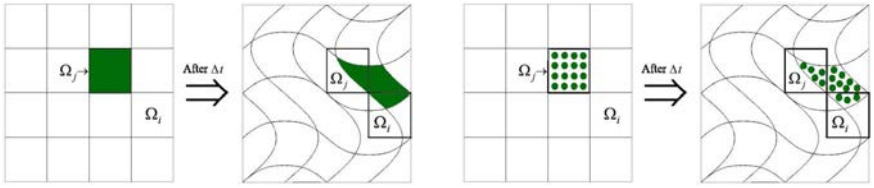

Figure 2: Computation of the mapping matrix from redistribution of material over a grid of finite mapping cells: (a) continuous (area-based) approach; (b) discrete (particle-based) approach.

mesh. The entries of the mapping matrix $\boldsymbol{\Xi}$ describing this redistribution are then given by

$$\Xi_{ij} = \frac{A_{ij}}{A_j}, \tag{5}$$

and represent the portion A_{ij} of the area of cell Ω_i received by cell Ω_j with area A_j. Normalization by recipient cell size and uniform cell sizes (typical situation) implies real entries $\Xi_{ij} \in [0, 1]$. This area-based mapping method is illustrated schematically in Figure 2(a).

Principal drawback of the above ansatz is that it entails tracking of continuous interfaces of material elements and determination of intersections of advected areas and cells, which is computationally expensive on account of the strong deformation of material elements in the course of the mixing process. A computationally more efficient way to evaluate the mapping matrix is by representation of the continuous material within cells by K discrete particles, as illustrated in Figure 2(b) [44]. The entries of the mapping matrix $\boldsymbol{\Phi}$ describing the period-wise particle redistribution over the cells are given by

$$\Phi_{ij} = \frac{M_{ij}}{M_j}, \tag{6}$$

with M_{ij} the number of the total amount of particles released in cell Ω_i and received by cell Ω_j. Here normalization takes place by the total number of particles M_j released in the recipient cell Ω_j. Thus particle amount M in (6) is entirely analogous to area A in the approach following (5). Entries are, as before, real and restricted to the interval $\Phi_{ij} \in [0, 1]$.

The mapping matrices $\boldsymbol{\Xi}$ and $\boldsymbol{\Phi}$ admit computation of the transport of arbitrary initial distributions $\boldsymbol{c}_0 \in R^{N\times 1}$ (or its discrete-particle representation) during each period via $\boldsymbol{c_1} = \boldsymbol{\Xi c}_0$ (or $\boldsymbol{c_1} = \boldsymbol{\Phi c}_0$), with $\boldsymbol{c_1} \in R^{N\times 1}$ the state after one period. This, in turn, facilitates efficient period-wise progression of initial states $\boldsymbol{c}_0$ by repetitive mapping following

$$\boldsymbol{c}_n = (\underbrace{\boldsymbol{\Xi}(\boldsymbol{\Xi}(...(\boldsymbol{\Xi}}_{\text{n times}}\boldsymbol{c}_0)...) = \boldsymbol{\Xi}^n\boldsymbol{c}_0 \qquad \Leftrightarrow \qquad \boldsymbol{c}_n = \boldsymbol{\Phi}^n\boldsymbol{c}_0, \tag{7}$$

with $\boldsymbol{c}_n$ the resulting distribution after n periods.

The above mapping approaches introduce departures from the continuous transport form (1). The finite cell size leaves sub-cell flow features unresolved. This manifests itself in "smearing-out" of distributions $\boldsymbol{c}_n$ over length scales comparable to the cell size in a diffusion-like manner. This "numerical diffusion" occurs for both $\boldsymbol{\Xi}$ and $\boldsymbol{\Phi}$ and diminishes with decreasing cell sizes, meaning it becomes insignificant for sufficiently large N. A further issue concerns mass conservation. Mapping matrix $\boldsymbol{\Xi}$ has column sums ($\sigma_j^c = \sum_i \Xi_{ij}$) as well as row sums ($\sigma_i^r = \sum_j \Xi_{ij}$) equal to unity (i.e. $\sigma_j^c = 1$ and $\sigma_i^r = 1$ for all $i, j \in [1, N]$). This signifies compliance with mass conservation by individual cells. Moreover, $\sum_{i=1}^N \sigma_i^r = \sum_{j=1}^N \sigma_j^c = N$ implies global mass conservation. Mapping matrix $\boldsymbol{\Phi}$, on the other hand, only has column sums equal to unity ($\sigma_j^c = 1$); row sums typically yield $\sigma_i^r \neq 1$ yet nonetheless meet $\sum_{i=1}^N \sigma_i^r = \sum_{j=1}^N \sigma_j^c = N$. Thus $\boldsymbol{\Phi}$ preserves mass only on a global level in that the *total* mass within the system remains constant while cell-wise mass contents may vary over time. (Physically, this is comparable to the presence of local sources and sinks that leave the total mass content unaffected.) Satisfaction of local mass conservation improves with growing K and becomes identical in the limit $K \to \infty$.

Two relevant cases must be distinguished concerning numerical diffusion and local violation of mass conservation: conformal and non-conformal mapping grids. Conformal mapping grids consist of cells that align with the transport barriers separating elliptic islands and chaotic seas (i.e. the outermost KAM tori of islands). Corresponding mapping matrices preserve the physical separation of these LCSs and, in consequence, numerical effects are confined to internal

transport within individual islands or chaotic seas. Non-conformal mapping grids, on the other hand, include cells that may cross the transport barriers and thus effectively "smear" the latter out into "fuzzy" boundaries, admitting manifestation of numerical diffusion on a global level.[5] Note that mapping grids typically are non-conformal.

Finite departures from local mass conservation, inherent in the particle-based representation (Section 2.2), manifest themselves in local non-conservative behaviour in a source-sink like manner and thus eradicate the Hamiltonian mechanisms that underly formation of LCSs in solenoidal flows [7, 38]. This has *grosso modo* the same impact on the correlation between true LCSs and their representation by the mapping matrix as numerical diffusion.

2.3. Eigenmode decomposition of the mapping matrix

The mapping matrices $\boldsymbol{\Xi}$ and $\boldsymbol{\Phi}$ constitute discrete approximations of the continuous Floquet operator $\mathcal{F}$ following (2) and admit representation as

$$\boldsymbol{\Phi} = \sum_{k=1}^{N} \lambda_k \boldsymbol{v}_k \boldsymbol{v}_k, \qquad \boldsymbol{\Xi} = \sum_{k=1}^{N} \lambda'_k \boldsymbol{v}'_k \boldsymbol{v}'_k \tag{8}$$

with $\{\boldsymbol{v}_k, \lambda_k\}$ and $\{\boldsymbol{v}'_k, \lambda'_k\}$ the corresponding eigenvector-eigenvalue pairs. Substitution of this form in mapping (7) yields

$$\boldsymbol{c}_n = \boldsymbol{\Phi}^n \boldsymbol{c}_0 = \sum_{k=1}^{N} \widetilde{c}_k^0 \boldsymbol{h}_k^{(n)}, \qquad \boldsymbol{h}_k^{(n)} = \lambda_k^n \boldsymbol{v}_k, \qquad \boldsymbol{c}_0 = \sum_{k=1}^{N} \widetilde{c}_k^0 \boldsymbol{v}_k, \tag{9}$$

as discrete approximation of the continuous eigenmode decomposition (3) by the particle-based matrix $\boldsymbol{\Phi}$. Here eigenvector-eigenvalue pairs $\{\boldsymbol{v}_k, \lambda_k\}$ and eigenmodes $\boldsymbol{h}_k^{(n)}$ are discrete counterparts to the eigenfunction-eigenvalue pairs $\{\Theta_k, \nu_k\}$ of the Floquet operator and the eigenmodes $\mathcal{H}_k^{(n)}$ in (3), respectively. The expansion coefficients $\widetilde{c}_k^0$, similar to coefficients γ_k in (3), are determined by the initial state $\boldsymbol{c}_0$. The corresponding eigenmode representation for $\boldsymbol{\Xi}$ is analogous and not shown for brevity.

[5] Realistic transport barriers are typically continuous and, in exceptional cases, may even be incomplete (e.g. cantori). These properties can not be exactly represented by finite cells. This rules out truly conformal mapping grids and implies that a certain degree of non-conformity is *always* present. This is considered negligible here for conceptual purposes, however.

Purely advective transport strictly confines the eigenvalue spectrum to the unit circle, i.e. $|\lambda_k| = 1$ for all k, implying a unitary mapping matrix [28, 29]. However, this condition is fulfilled only in the hypothetical case of infinite spatial resolution, or equivalently, a conformal mapping grid perfectly coinciding with the ergodic partition of the Lagrangian flow structure. Actual mapping matrices suffer from numerical diffusion due to finite cell sizes, resulting in local smearing-out of spatial features (Section 2.2). This, in turn, causes the spectrum to (partially) fall within the unit circle in a similar manner as for Floquet operators with finite Pe [44]. The eigenmodes of the actual mapping matrix nonetheless are physically meaningful in that they constitute slightly "fuzzied" representations of the eigenmodes of the ideal unitary mapping matrix. Moreover, the diffusion-like behavour in fact adequately represents the weak yet inevitable molecular diffusion in any real flow (Section 2.1)

The study by Singh *et al.* [34] revealed that the properties of the eigenmodes of $\mathbf{\Phi}$ correlate with the LCSs formed by fluid trajectories and has been exemplified in Section 2.1 by way of the TSPF. The key findings have been condensed in the following conjectures:

Conjecture 1. *Elliptic islands relate to eigenmodes with* $|\lambda_k| = 1$.

Conjecture 2. *Chaotic seas have eigenmodes with* $|\lambda_k| < 1$.

Conjecture 3. *Eigenmodes of elliptic islands and chaotic seas are spatially disconnected.*

Conjecture 4. *Period-p structures of equal kind correspond with clusters of eigenvalues* $\left\{\lambda^{(0)}, \lambda^{(1)}, \ldots, \lambda^{(m)}, \ldots, \lambda^{(p-1)}\right\}$, *with* $\lambda^{(m)} = |\lambda|\omega^m$ *and* $\omega = e^{\frac{2\pi i}{p}}$.

Conjecture 5. *The eigenvectors corresponding with eigenvalues as per Conjecture 4 combined demarcate the invariant region occupied by the entire period-p group.*

Note that the original statement of Conjecture 5 following [34] has been reformulated here yet with retention of its meaning. These conjectures imply that

eigenmodes, apart from the trivial eigenmode, always group into the following three categories:

1. persistent eigenmodes ($|\lambda_k| = 1$) associated with elliptic islands;
2. decaying eigenmodes ($|\lambda_k| < 1$) associated with elliptic islands;
3. decaying eigenmodes ($|\lambda_k| < 1$) associated with chaotic seas.

Eigenvalues $|\lambda_k| \leq 1$ invariably cause progression of any initial state to an asymptotic state determined by the persistent eigenmodes. The decaying eigenmodes dictate the transient towards that state; their exponential decay in magnitude means that (local) transients rapidly become dominated by the slowest-decaying eigenmode in a given region, that is, the decaying eigenmode with the highest $|\lambda_k| < 1$ ("dominant eigenmode") [34]. Figure 3 shows typical examples of the above kinds of eigenmodes for the TPSF at $T = 0.8$. The eigenmodes associated with elliptic islands and chaotic sea (panels (a)-(c)) are evidently non-zero only within these LCSs (compare with the Poincaré section in Figure 1(b)).

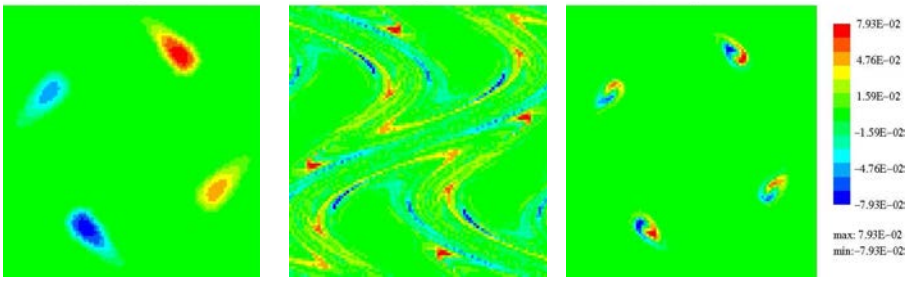

(a) (b) (c)

Figure 3: Three kinds of eigenmodes in the mapping matrix $\mathbf{\Phi}$ demonstrated for the TPSF ($T = 0.8$): (a) persistent eigenmode of elliptic islands; (b) decaying eigenmode of chaotic sea; (c) decaying eigenmode of elliptic islands.

The above categorisation of eigenmodes – and the underlying Conjectures 1-5 – pertains specifically to conformal mapping grids. The stringent separation between LCSs means that inhomogeneous concentration distributions due to entrapment of material within elliptic islands are maintained indefinitely. This implies the above persistent eigenmodes. The accompanying decaying eigenmodes

emanate from localized smearing-out due to non-conformity of the mapping grid with internal KAM tori. Emergence of only decaying eigenmodes in the chaotic seas stems from the fact that here spatial features are infinitely small and of great geometrical complexity, leading to non-conformity – and smearing-out – throughout the *entire* region. Non-conformal grids introduce small departures from this scenario in that *all* eigenvalues, save the trivial eigenmode associated with global mass conservation, move inside the unit circle. However, this effect is marginal for sufficient (yet feasible) spatial resolutions, meaning that the above properties are retained to a high degree of accuracy [44]. The close agreement between the eigenmodes in Figure 3, obtained by a non-conformal mapping grid, and the corresponding Poincaré sections is testament to this. Furthermore, recall from the previous that the numerical diffusion underlying this localized smearing-out in fact represents a physically-meaningful phenomenon.

The particular association between LCSs and eigenmodes for conformal grids fundamentally determines its composition. This is explored in Section 3. Changes in this composition brought on by employing non-conformal mapping grids are discussed in Section 4.

3. Composition of the mapping matrix for conformal grids

3.1. Introduction

The distinction of three fundamental kinds of eigenmodes for mapping matrices built with conformal grids implies a generic decomposition into three invariant eigenspaces following

$$\boldsymbol{\Phi} = \sum_{k\in\mathcal{K}_1} \lambda_k^{(1)} \boldsymbol{v}_k^{(1)} \boldsymbol{v}_k^{(1)} + \sum_{k\in\mathcal{K}_2} \lambda_k^{(2)} \boldsymbol{v}_k^{(2)} \boldsymbol{v}_k^{(2)} + \sum_{k\in\mathcal{K}_3} \lambda_k^{(3)} \boldsymbol{v}_k^{(3)} \boldsymbol{v}_k^{(3)}, \tag{10}$$

with superscripts referring to the categories introduced before and $\mathcal{K}_i$ the corresponding subspectrum, where $\mathcal{K}_1 \cup \mathcal{K}_2 \cup \mathcal{K}_3 \in [1, N]$. Mapping matrices $\boldsymbol{\Xi}$ and $\boldsymbol{\Phi}$ both have non-negative entries ($\Xi_{ij} \geq 0$ and $\Phi_{ij} \geq 0$) and column sums equal to unity (Section 2.2); this renders them so-called *stochastic matrices* [45]. Furthermore, redistribution of material by the mapping matrix over the cells is essentially the same as generic flows in networks and thus admits representation

by graphs. These properties have essential consequences for their structures and the associated transport characteristics.

3.2. Graph representation of the mapping matrix

The mapping matrix can be thought of as an adjacency matrix of a graph with weighted and directed edges. This means that every cell $i = 1, 2, ..., N$ in the mapping grid corresponds with a vertex of graph $G(\mathbf{\Phi})$. Every nonzero entry Φ_{ij} indicates that there is a directed edge from vertex j to vertex i. This edge has weight Φ_{ij} and, because $\mathbf{\Phi}$ may be asymmetric, the edge from i to j can have a different weight than the edge from j to i. The graph $G(\mathbf{\Phi})$ visualizes the redistribution of material over the entire domain within the course of one period. Figure 4 illustrates this graph representation of mapping matrices by way of a mapping mesh consisting of four cells and

$$\mathbf{\Phi} = \begin{bmatrix} \Phi_{11} & \Phi_{12} & 0 & 0 \\ \Phi_{21} & \Phi_{22} & \Phi_{23} & \Phi_{24} \\ \Phi_{31} & 0 & 0 & \Phi_{34} \\ 0 & 0 & \Phi_{43} & 0 \end{bmatrix} \tag{11}$$

as the corresponding mapping matrix. Non-zero diagonal elements Φ_{ii} indicate retention of material within cell i and emerge as a self-loop in the graph (here e.g. for cells $i = 1, 2$). Isolated zero entries Φ_{ij} imply absence of direct material transfer from cell j to cell i yet not necessarily *vice versa* (e.g. $i = 1$ and $j = 3$); diagonally-opposite zero entries ($\Phi_{ij} = \Phi_{ji} = 0$) reflect total absence of material exchange between cells i and j (e.g. $i = 1$ and $j = 4$). Material in cell i is after p periods distributed over cells (vertices) that are maximally p steps away in the graph. This means that full redistribution over all cells is either achieved in at most $p = N$ periods, manifesting itself in absence of zero entries in $\mathbf{\Phi}' = \mathbf{\Phi}^N$, or never at all. Note $\mathbf{\Phi}'$ for $\mathbf{\Phi}$ following (11) is indeed devoid of such entries, signifying full redistribution. This also follows from the graph.

3.3. Block-diagonal structure of the mapping matrix

The above has the important implication that occurrence of any $\Phi'_{ij} = \Phi'_{ji} = 0$ implies disconnected subgraphs, which, in turn, signifies the presence of trans-

port barriers in the underlying physical domain. In that case the mapping matrix admits transformation in a block-diagonal structure, where each block corresponds to a subregion in the graph (and physical domain) that is physically-separated from the rest. Consider to this end

$$\boldsymbol{\Phi} = \begin{bmatrix} \Phi_{11} & 0 & \Phi_{13} & 0 \\ 0 & \Phi_{22} & 0 & \Phi_{24} \\ \Phi_{31} & 0 & \Phi_{33} & 0 \\ 0 & \Phi_{42} & 0 & \Phi_{44} \end{bmatrix} \quad \Rightarrow \quad \boldsymbol{\Phi}'' = \begin{bmatrix} \Phi_{11} & \Phi_{13} & 0 & 0 \\ \Phi_{31} & \Phi_{33} & 0 & 0 \\ 0 & 0 & \Phi_{22} & \Phi_{24} \\ 0 & 0 & \Phi_{42} & \Phi_{44} \end{bmatrix} \tag{12}$$

as alternative to (11). Here only material transfer takes place *within* yet not *between* the cell groups $\{1, 3\}$ and $\{2, 4\}$. This exposes a physical separation between both groups and, in consequence, admits transformation of $\boldsymbol{\Phi}$ in given block-diagonal structure $\boldsymbol{\Phi}''$ via straightforward row/column permutations.

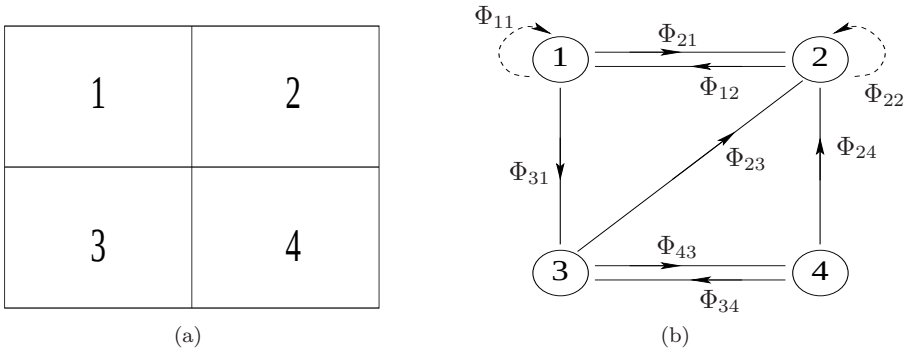

Figure 4: Graph representation of the mapping method: (a) mapping grid; (b) graph representing mapping matrix (11).

The presence of KAM tori in generic transport systems implies physical separation of flow regions and, inherently, of groups of cells (Conjecture 3). This means that the (conformal-grid) mapping matrix in general admits transformation in a block-diagonal structure via

$$\boldsymbol{\Phi} \quad \Rightarrow \quad \boldsymbol{\Phi}'' = \boldsymbol{P}\boldsymbol{\Phi}\boldsymbol{P}^T = \begin{bmatrix} \boldsymbol{A}_1 & \mathbf{0} & \dots & \mathbf{0} \\ \mathbf{0} & \boldsymbol{A}_2 & \dots & \mathbf{0} \\ \vdots & \vdots & \ddots & \vdots \\ \mathbf{0} & \mathbf{0} & \dots & \boldsymbol{A}_k \end{bmatrix} \tag{13}$$

by way of a permutation $\boldsymbol{P}$. Here each block $\boldsymbol{A}_k$, which is completely decoupled from all other blocks, corresponds with the groups of cells covering a distinct LCS, defined by (clusters of) elliptic islands or chaotic seas. The eigenvalue-eigenvector pairs of the blocks combined span the eigenspace of $\boldsymbol{\Phi}$. Block-diagonal structure (13) is intimately related to the modal structure (10) and the underlying Conjecture 3 in that eigenmode sets $\mathcal{K}_{1,2}$ (islands) and $\mathcal{K}_3$ (chaotic seas), if present, belong to different blocks. Both sets admit further subdivision into blocks in case of multiple LCSs of the same type. This is demonstrated for the multiple islands in the TPSF at $T = 0.56$ in Section 5.

The underlying block-diagonal structure (13) imparts itself on the structure of the mapping matrix. Introduce to this end the matrix functional $\boldsymbol{Z}(\boldsymbol{M})$, with $Z_{ij} = 0$ and $Z_{ij} = 1$ if $|M_{ij}| = 0$ and $|M_{ij}| > 0$, respectively. Its application to the mapping matrix $\boldsymbol{\Phi}$ yields

$$\boldsymbol{Z}(\boldsymbol{\Phi}) = \boldsymbol{Z}(\boldsymbol{\Phi}^T) = \boldsymbol{Z}(\boldsymbol{\Phi}'), \tag{14}$$

implying that $\boldsymbol{\Phi}$ identically adopts the beforementioned symmetric arrangement of zero and non-zero entries of $\boldsymbol{\Phi}'$ that, in turn, signifies the presence of transport barriers.[6] Hence, such barriers, if existent, leave a distinct footprint directly in the mapping matrix $\boldsymbol{\Phi}$. Conversely, this means that their existence *perse* can be readily inferred from the mapping matrix in that *any* diagonally-opposite zero entries signify transport barriers. (Note that this includes KAM tori within islands upon sufficient local conformity of the grid.) Their actual demarcation in the flow domain directly from $\boldsymbol{\Phi}$ is non-trivial, however.

It must be stressed that the block-diagonal structure according to (13) is essentially different from a diagonalisation (or its generalisation, the Jordan canonical form [46]) by a similarity transform based on eigenvectors. The latter typically overlap (partially) in the physical domain and thus violate Conjecture 3. Transformation (13), on the other hand, leans on decomposition into

[6] These conditions readily follow from $\boldsymbol{Z}(\boldsymbol{\Phi}^T) = [\boldsymbol{P}^T\boldsymbol{Z}(\boldsymbol{\Phi}'')\boldsymbol{P}]^T = \boldsymbol{P}^T\boldsymbol{Z}(\boldsymbol{\Phi}''^T)\boldsymbol{P} = \boldsymbol{P}^T\boldsymbol{Z}(\boldsymbol{\Phi}'')\boldsymbol{P} = \boldsymbol{Z}(\boldsymbol{\Phi})$ and $\boldsymbol{Z}(\boldsymbol{\Phi}') = \boldsymbol{P}^T\boldsymbol{Z}(\boldsymbol{\Phi}''^N)\boldsymbol{P} = \boldsymbol{P}^T\boldsymbol{Z}(\boldsymbol{\Phi}'')\boldsymbol{P} = \boldsymbol{Z}(\boldsymbol{\Phi})$ due to properties $\boldsymbol{Z}(\boldsymbol{\Phi}'') = \boldsymbol{Z}(\boldsymbol{\Phi}''^T) = \boldsymbol{Z}(\boldsymbol{\Phi}''^N)$, $\boldsymbol{P}\boldsymbol{P}^T = \boldsymbol{I}$ and $\boldsymbol{Z}(\boldsymbol{P}) = \boldsymbol{P}$.

spatially-separated groups of eigenvectors by reordering of cells. Determination of the permutation matrix $\boldsymbol{P}$ may hinge on a Gaussian-like elimination procedure applied to $\boldsymbol{Z}(\boldsymbol{\Phi})$; development of an algorithm is beyond the present scope, however.

The generic mapping matrix of a given flow is assembled from matrices $\boldsymbol{A}_k$ that each represent (clusters of) elliptic islands and chaotic seas. Each $\boldsymbol{A}_k$ in fact constitutes a mapping matrix in its own right for a specific flow region. The composition of the blocks depends on the associated Lagrangian flow structure. This is elaborated in the following section.

3.4. Block composition: elementary matrices

Mapping matrices $\boldsymbol{\Xi}$ and $\boldsymbol{\Phi}$ both constitute stochastic matrices on grounds on non-negative entries and column sums equal to unity (Section 3.1). Matrix $\boldsymbol{\Xi}$ furthermore has row sums equal to unity and thus defines a *doubly-stochastic matrix* [45]. This has the important consequence that each vertex (cell) of the corresponding graph must have both incoming edges and outgoing edges. (This is in fact the generalisation of Kirchhoff's circuit laws for current flows in electrical circuits [47].) Note that this does not entail full connectivity of all cells; disconnected subgraphs, or equivalently, physical division of the flow domain in subregions is still possible. Moreover, since $\lim_{K\to\infty} \boldsymbol{\Phi} = \boldsymbol{\Xi}$, this property (to good approximation) carries over to $\boldsymbol{\Phi}$ for sufficient seeding density K (Section 2.2).

The connection with (doubly-)stochastic matrices enables further exploration of the composition of the mapping matrix using general matrix theory. To this end properties relevant in the current context are recapitulated below [45, 46, 48].

Property 1. *Any stochastic matrix has conjugate complex eigenvalues* $|\lambda_k| \leq 1$ *and at least one eigenvalue* $\lambda_k = 1$ *(Perron-Frobenius theorem).*

This implies a multiplicity of eigenvalue $\lambda_k = 1$ that is at least equal to the number of blocks. Hence, such multiplicity may indicate – yet not conclusively

establish – the existence of disconnected flow regions. Property 1 is consistent with the fact that the mapping matrix only admits persistent ($|\lambda_k| = 1$) and decaying ($|\lambda_k| < 1$) eigenmodes (Section 2.3). This advances permutation matrices $\mathbf{\Pi}$ and regular (doubly-)stochastic matrices $\boldsymbol{D}$ as elementary building blocks of mapping matrices, which is elaborated below.

Permutation matrices $\mathbf{\Pi}$ consist of entries equal to either zero or unity such that each column and row has only one non-zero element. Hence, each $\mathbf{\Pi}$ is in fact a permutation of the unit matrix $\boldsymbol{I}$ and thus defines a doubly-stochastic matrix. Thus a permutation matrix $\mathbf{\Pi}$ effectuates either complete or no transport of material from cell j to cell i: $\Phi_{ij} = 1$ or $\Phi_{ij} = 0$. Furthermore, this transport is such that *each* cell i transfers its material entirely to one companion cell j; division over multiple cells does not occur. This implies:

Property 2. *Permutation matrices* $\mathbf{\Pi}$ *have determinant* $\det(\mathbf{\Pi}) = \pm 1$ *and eigenvalues* $|\lambda_k| = 1$. *The associated graph admits at least one directed cycle without self-loops.*

Property 3. *Permutation matrices* $\mathbf{\Pi}$ *are periodic:* $\mathbf{\Pi}^{p+k} = \mathbf{\Pi}^p$ *and* $\mathbf{\Pi}^k = \boldsymbol{I}$ *for all* $p \geq 1$ *and some periodicity* $k \geq 1$.

Property 4. *The (possibly repeated) eigenvalues of a permutation matrix with periodicity* k *are restricted to the* k *complex roots of unity:* $\lambda_k \in [1, \omega, \omega^2, \ldots, \omega^{k-1}]$.

Here $\omega = e^{2\pi i/k}$ and $i = \sqrt{-1}$. Note that the eigenvalue spectrum must not include all elements in this set; only $\lambda = 1$ is invariably present by virtue of Property (1).

Properties 2-4 imply two kinds of transport: (i) indefinite redistribution of material within cell groups; (ii) cyclic redistribution of material between cell groups. Former and latter scenarios respectively correspond to the action of persistent eigenmodes and the progression of material through coherent structures associated with clusters of periodic points (e.g. island chains). Thus persistent eigenmodes, and by virtue of Conjecture 1, islands as well as generic

higher-order periodic structures imply permutation matrices or permutation-like organization within the mapping matrix. This is worked out in Sections 3.5 and 3.6. Moreover, Property 4 cements Conjecture 4 and, given that (clusters of) coherent structures correspond with block matrices $\boldsymbol{A}$ and thus non-overlapping eigenvectors (Section 3.3), indirectly also Conjecture 5.

Regular (doubly-)stochastic matrices $\boldsymbol{D}$ are characterized by the property that $\boldsymbol{D}' = \boldsymbol{D}^k$, with k a given (finite) number of periods, consists entirely of non-zero elements: $D'_{i,j} > 0$ for all $i, j \in [1, N]$. This means that after k periods *each* cell has exchanged material with *all* cells (including itself) within the mapping mesh. The corresponding graph G connects any two cells i and j with a directed walk of at most length k. Hence, material from cell i reaches any cell j within at most k periods. Relevant properties are:

Property 5. *A regular stochastic matrix $\boldsymbol{D}$ has conjugate complex eigenvalues $|\lambda_k| < 1$ and one isolated eigenvalue $\lambda_k = 1$.*

Property 6. *A regular stochastic matrix $\boldsymbol{D}$ has a unique limit $\lim_{n\to\infty} \boldsymbol{D}^n = \boldsymbol{L}$. Each column of $\boldsymbol{L}$ is identical to the (normalized) eigenvector $\boldsymbol{e}$ of the isolated eigenvalue $\lambda_k = 1$.*

Property 7. *Eigenvector $\boldsymbol{e}$ is proportional to the unit vector ($\boldsymbol{e} = N^{-1}\mathbf{1}$) for $N \times N$ doubly-stochastic regular matrices.*

These properties imply that the progression of any given initial state $\boldsymbol{c}_0$ converges on an asymptotic state proportional to $\boldsymbol{e}$: $\lim_{n\to\infty} \boldsymbol{D}^n \boldsymbol{c}_0 \propto \boldsymbol{e}$. Said state is homogeneous in case of doubly-stochastic regular matrices (as e.g. $\boldsymbol{\Xi}$). This corresponds to the action of decaying eigenmodes. Chaotic seas are dictated entirely by such modes, meaning that corresponding block matrices in (13) are composed exclusively of regular (doubly-)stochastic matrices $\boldsymbol{D}$. Hence, Property 5 substantiates Conjecture 2. Transport within islands, on the other hand, is governed by an interplay of both persistent and decaying eigenmodes; here block matrices thus are composed of permutation and regular stochastic matrices. The ramifications for the composition of actual mapping matrices are

addressed in Sections 3.5 and 3.6.

Figure 5 gives a simple illustration of both matrix types for a 4-cell mesh with matrices

$$\boldsymbol{\Pi} = \begin{bmatrix} 1 & 0 & 0 & 0 \\ 0 & 0 & 1 & 0 \\ 0 & 1 & 0 & 0 \\ 0 & 0 & 0 & 1 \end{bmatrix}, \qquad \boldsymbol{D} = \begin{bmatrix} \frac{1}{2} & 0 & \frac{1}{2} & 0 \\ 0 & 0 & \frac{1}{2} & \frac{1}{2} \\ \frac{1}{4} & \frac{3}{4} & 0 & 0 \\ \frac{1}{4} & \frac{1}{4} & 0 & \frac{1}{2} \end{bmatrix}. \tag{15}$$

Matrix $\boldsymbol{\Pi}$ has periodicity $k = 2$ and the initial state is restored identically after two periods: $\boldsymbol{\Pi}^2 = \boldsymbol{I}$. Matrix $\boldsymbol{D}^3$ has only nonzero entries, meaning that each cell has exchanged material with every other cell (including itself) after $k = 3$ periods. Furthermore, matrix $\boldsymbol{D}$ has a limit following Property 6 and corresponding columns $\boldsymbol{e} = [1/4\ 1/4\ 1/4\ 1/4]$) as per Property 7. This ensures that redistribution by matrix $\boldsymbol{D}$ results in homogenisation of any initial state.

3.5. Block composition: period-1 chaotic seas and elliptic islands

Periodic points are the organizing entities of the Lagrangian flow structure: period-1 points yield isolated LCSs; higher-order periodic points (periodicity $p > 1$) result in clusters of LCSs (Section 2.1). The above reconciled LCSs with two elementary matrices, i.e. permutation matrices and regular stochastic matrices, which fundamentally determines the composition of the block matrices $\boldsymbol{A}$ in (13). The remainder of this section treats this composition for the period-1 case; Section 3.6 continues with higher-order cases.

The evolution within chaotic seas is dictated solely by decaying eigenmodes and in Section 3.4 has been tied to regular stochastic matrices $\boldsymbol{D}$. Hence, blocks $\boldsymbol{A}_k$ in (13) emanating from period-1 chaotic seas simply adopt the structure of said matrix type, viz.

$$\boldsymbol{A}_k = \boldsymbol{D}_k, \qquad \boldsymbol{A}_{k,\infty} = \lim_{n\to\infty} \boldsymbol{A}_k^n = \boldsymbol{L}, \tag{16}$$

and directly inherit Properties 5-7.

The case of period-1 islands is more involved in that transport ensues from an interplay of decaying and persistent eigenmodes. Performance of a local similarity transform yields

$$\boldsymbol{V}_k^{-1}\boldsymbol{A}_k\boldsymbol{V}_k = \boldsymbol{\Lambda}_k = \begin{bmatrix} \boldsymbol{\Lambda}_\Pi & \boldsymbol{0} \\ \boldsymbol{0} & \boldsymbol{\Lambda}_D \end{bmatrix}, \tag{17}$$

with matrices $\boldsymbol{V}_k$ and $\boldsymbol{\Lambda}_k$ containing the eigenvectors and eigenvalues, respectively, of $\boldsymbol{A}_k$. Ordering is such that the eigenvalue spectrum is separated into persistent modes $|\lambda_i| = 1$ (held in $\boldsymbol{\Lambda}_\Pi$) and decaying modes $|\lambda_i| < 1$ (held in $\boldsymbol{\Lambda}_D$). Matrices $\boldsymbol{\Lambda}_\Pi$ and $\boldsymbol{\Lambda}_D$ are basically diagonalized representations of permutation and regular stochastic matrices $\boldsymbol{\Pi}$ and $\boldsymbol{D}$, respectively. Primary difference is that the latter has the trivial limit $\lim_{n\to\infty}\boldsymbol{\Lambda}_D^n = \boldsymbol{0}$ due to the absence of an eigenvalue equal to unity. This has the important consequence that matrix $\boldsymbol{A}_k$ asymptotes toward the "pseudo-permutation" matrix

$$\boldsymbol{\Pi}_k = \lim_{n\to\infty}\boldsymbol{A}_k^n, \qquad \boldsymbol{\Pi}_k = \boldsymbol{V}_k\boldsymbol{\Lambda}_{k,\infty}\boldsymbol{V}_k^{-1} = \boldsymbol{\Pi}_k^p, \qquad \boldsymbol{\Lambda}_{k,\infty} = \begin{bmatrix} \boldsymbol{\Lambda}_\Pi & \boldsymbol{0} \\ \boldsymbol{0} & \boldsymbol{0} \end{bmatrix}, \tag{18}$$

with p some periodicity.[7] The gradual diminution of contribution $\boldsymbol{\Lambda}_D^n$ paves the way to indefinite periodic redistribution of material within the cell group by $\boldsymbol{\Lambda}_\Pi = \boldsymbol{\Lambda}_\Pi^p$; this physically corresponds with the progression towards cyclically recurring persistent patterns within islands [34]. Note that typically $p > 1$; periodicity p namely concerns permutation of the individual cells within the period-1 island and not the island as a whole.

3.6. Block composition: higher-order periodicity

3.6.1. Clusters of elliptic islands

Transport within clusters of elliptic islands can be exemplified by way of the asymptotic state, described by pseudo-permutation matrices (18), without loss of generality. Moreover, their action is in essence equivalent to that of true

[7] Note that $\boldsymbol{\Pi}_k$, strictly, is not a true permutation matrix, since it accommodates null modes. However, these modes yield no contribution to the scalar field in the asymptotic limit, as these have diminished on account of the decaying modes. Hence, in this reduced eigenspace, $\boldsymbol{\Pi}_k$ acts as a true permutation matrix.

permutation matrices. The latter acts on individual cells; the former acts on groups of cells corresponding with persistent eigenmodes of $\boldsymbol{A}_k$. Consider to this end e.g. the asymptotic state within a cluster of period-2 islands. The cluster as a whole consists of 8 cells, 4 cells for island A and 4 cells for island B (Figure 6(a)). The corresponding graph in case $\boldsymbol{\Pi}_A = \boldsymbol{\Pi}_B = \boldsymbol{\Pi}$ following (15) is in Figure 6(b). Here the two kinds of transport associated with permutations, identified in Section 3.4, occur simultaneously: (i) redistribution within each island by 4×4 permutation matrices $\boldsymbol{\Pi}_A$ and $\boldsymbol{\Pi}_B$; (ii) periodic exchange of material between the islands by a permutation that fully exchanges the 4 cells covering islands A and B. This implies that transport and mixing is described by an 8×8 mapping matrix

$$\boldsymbol{A} = \begin{bmatrix} \mathbf{0} & \boldsymbol{\Pi}_A \\ \boldsymbol{\Pi}_B & \mathbf{0} \end{bmatrix}, \tag{19}$$

with $\boldsymbol{\Pi}_A$ and $\boldsymbol{\Pi}_B$ two 4×4 permutation matrices. Important to note is that (19) has a permutation structure, say it that non-zero regions comprise elementary submatrices instead of individual entries. Hence, "nested permutations" exist here in that permutation happens concurrently on both intra-island and inter-island level. The period-2 behaviour manifests itself in the block-diagonal structure

$$\boldsymbol{A}^{2p} = \begin{bmatrix} (\boldsymbol{\Pi}_A \boldsymbol{\Pi}_B)^p & \mathbf{0} \\ \mathbf{0} & (\boldsymbol{\Pi}_B \boldsymbol{\Pi}_A)^p \end{bmatrix} \qquad \forall p \geq 1, \tag{20}$$

reflecting the invariance of the island cluster *as a whole* every two cycles yet with continuous *internal* redistribution by action of $\boldsymbol{\Pi}_A \boldsymbol{\Pi}_B$ and $\boldsymbol{\Pi}_B \boldsymbol{\Pi}_A$. This is fully consistent with the behaviour in clusters of elliptic islands in actual mixing flows (Section 2.1).

The above admits generalisation to clusters of period-k islands $\mathcal{I}_1 \cup \mathcal{I}_2 \cup \cdots \cup \mathcal{I}_k$. Essential to such clusters is that material contained in a given island $\mathcal{I}_p$ is always fully mapped to a companion island during each mapping. Ordering islands (and its corresponding groups of cells) such that material progresses through the cluster via $\mathcal{I}_1 \to \mathcal{I}_2 \to \cdots \to \mathcal{I}_k$ yields a corresponding graph on the

inter-island level that forms a directed cycle (Property 2) following the schematic in Figure 6(c). Thus the associated inter-island mapping matrix collapses on the generic form

$$\boldsymbol{A} \;=\; \begin{bmatrix} \mathbf{0} & \boldsymbol{\Pi}_1 & & & \\ \vdots & \mathbf{0} & \boldsymbol{\Pi}_2 & & \\ \vdots & & \ddots & \ddots & \\ \mathbf{0} & & & \mathbf{0} & \boldsymbol{\Pi}_{k-1} \\ \boldsymbol{\Pi}_k & \mathbf{0} & \cdots & \cdots & \mathbf{0} \end{bmatrix}, \tag{21}$$

with $\boldsymbol{\Pi}_p$ the intra-island permutation matrices. The period-k behaviour emanates from Property 3 and manifests itself in a block-diagonal structure

$$\boldsymbol{A}^k \;=\; \begin{bmatrix} \prod_{p=1}^{k} \boldsymbol{\Pi}_p & & & \\ & \prod_{p=1}^{k} \boldsymbol{\Pi}_{p+1} & & \\ & & \ddots & \\ & & & \prod_{p=1}^{k} \boldsymbol{\Pi}_{p+k-1} \end{bmatrix}, \tag{22}$$

where $\boldsymbol{\Pi}_{k+i} = \boldsymbol{\Pi}_i$ on grounds of the closed loop formed by the islands, reflecting the invariance of the island cluster as a whole. The matrix product in each block represents the continuous intra-island redistribution. The clusters of period-k islands thus, similar to the previous example, possess the same two levels of permutation: intra-island and inter-island permutations.

The inter-island permutation manifests itself in a particular "spectral footprint." Factorise $\boldsymbol{A}$ to this end in

$$\boldsymbol{A} = \boldsymbol{\Pi}_* \boldsymbol{A}_*, \quad \boldsymbol{\Pi}_* = \begin{bmatrix} \mathbf{0} & \boldsymbol{I}_* & \dots & \mathbf{0} \\ \vdots & \ddots & \ddots & \\ \mathbf{0} & \dots & \mathbf{0} & \boldsymbol{I}_* \\ \boldsymbol{I}_* & \mathbf{0} & \dots & \mathbf{0} \end{bmatrix}, \quad \boldsymbol{A}_* = \begin{bmatrix} \boldsymbol{\Pi}_1 & & \\ & \ddots & \\ & & \boldsymbol{\Pi}_k \end{bmatrix}, \tag{23}$$

with $\boldsymbol{I}_*$ the block-size unit matrix.[8] Thus $\boldsymbol{A}$ consists of the product of the

[8] Permutation matrix $\boldsymbol{\Pi}_*$ can be defined only for blocks of equal size; otherwise factorisation (23) adopts a tensor structure. (This is beyond the present scope). Block structures (21) and (22) are always valid.

block-permutation matrix $\mathbf{\Pi}_*$, with periodicity k (i.e. $\mathbf{\Pi}_*^k = \boldsymbol{I}$), and the block-diagonal matrix $\boldsymbol{A}_*$, with permutation matrices as diagonal elements. Consider for simplicity all blocks of size $K \times K$. Eigenvalues of $\mathbf{\Pi}_*$ can for this particular permutation be shown to identify with the *full* set $\mathcal{P}(k) = [1, \omega, \omega^2, \ldots, \omega^{k-1}]$, where $\omega = e^{2\pi i/k}$ (Property 4), with multiplicity K. Periodicities – and thus the corresponding eigenvalue spectra – of the individual matrices $\mathbf{\Pi}_i$ may vary yet two conditions are always met. First, $|\lambda_k| = 1$ (Property 2) for each $\mathbf{\Pi}_i$, meaning all eigenvalues of $\boldsymbol{A}$ sit on the unit circle $|\lambda| = 1$ in the complex plane spanned by $(Re(\lambda), Im(\lambda))$. Second, at least one eigenvalue $\lambda_k = 1$ exists for each $\mathbf{\Pi}_i$ (Property 1). This implies k eigenvectors $\boldsymbol{v}_i$ of $\boldsymbol{A}_*$ that are invariant under its action: $\boldsymbol{A}_*\boldsymbol{v}_i = \boldsymbol{v}_i$. These eigenvectors span a subspace $\mathcal{V} = [\boldsymbol{v}_1, \ldots, \boldsymbol{v}_k]$ of the column space of $\boldsymbol{A}$ within which the latter acts as a permutation matrix, i.e. $\boldsymbol{A}\boldsymbol{w} = \mathbf{\Pi}_*\boldsymbol{w}$ for $\boldsymbol{w} \in \mathcal{V}$, due to $\boldsymbol{A}\boldsymbol{v}_i = \mathbf{\Pi}_*\boldsymbol{v}_i$. (Note that $\boldsymbol{v}_i$ are not eigenvectors of $\boldsymbol{A}$ or $\mathbf{\Pi}_*$.) Thus the spectrum of $\boldsymbol{A}$ includes the k eigenvalues $\mathcal{P}(k)$ associated with the permutation matrix $\mathbf{\Pi}_*$. Set $\mathcal{P}(k)$ constitutes the "signature" of the permutation and is denoted "permutation set" hereafter. Its presence in the eigenvalue spectrum of $\boldsymbol{A}$ further consolidates Conjecture 4 (Section 2.3).

A special case exists in repeated block matrices $\mathbf{\Pi}_1 = \mathbf{\Pi}_2 = \cdots = \mathbf{\Pi}_k = \mathbf{\Pi}$, which causes k-fold repetition of $\mathcal{Q} = eig(\mathbf{\Pi})$ ("parent spectrum") in the spectrum of $\boldsymbol{A}_*$. This, on similar grounds as before, subdivides the column space of $\boldsymbol{A}$ into k subspaces $\mathcal{V}_i$, each spanned by eigenvectors belonging to identical eigenvalues λ_i, within which $\boldsymbol{A}$ acts as $\boldsymbol{A}\boldsymbol{w} = \lambda_i\mathbf{\Pi}_*\boldsymbol{w}$. The generic matrix property $eig(\alpha\boldsymbol{B}) = \alpha\, eig(\boldsymbol{B})$ then leads to

$$eig(\boldsymbol{A}) = \mathcal{P}(k) \times \mathcal{Q}, \tag{24}$$

defined by the product of the spectra of its factors $\mathbf{\Pi}_*$ and $\boldsymbol{A}_*$. The spectral footprint of $\boldsymbol{A}$ thus results from k-fold permutation of parent spectrum $\mathcal{Q}$ by the permutation set $\mathcal{P}(k)$, or equivalently, K-fold mapping of $\mathcal{P}(k)$. This is exemplified for $\mathbf{\Pi}$ following (15) and $k = 3$ as periodicity of $\mathbf{\Pi}_*$. Here $\mathcal{P}(k) = [1, \omega, \omega^2]$, with $\omega = e^{2\pi i/3}$, and $\mathcal{Q} = [1, 1, 1, -1]$, yielding $eig(\boldsymbol{A}) = [1, \omega, \omega^2, 1, \omega, \omega^2, 1, \omega, \omega^2, -1, -\omega, -\omega^2]$. Figure 7(a) gives the corresponding

representation in the complex plane. Here stars indicate the parent spectrum $\mathcal{Q}$; circles and crosses indicate permutations by ω and ω^2, respectively. The star-circle-cross sequence starting from $\lambda = 1$ coincides with the permutation spectrum $\mathcal{P}(k)$. The spectrum for transient states is equivalent in the sense that form (24) is retained yet with parent spectrum also including $|\lambda| < 1$ associated with decaying modes. The spectral footprint is essentially as shown in Figure 7(a), expanded by modes within the unit circle.

The existence of distinct spectral footprints in principle facilitates isolation of clusters of islands in the total eigenvalue spectrum of the mapping matrix and this approach has found first applications in Singh *et al.* [34] However, multiplicity and restriction of persistent modes to the unit circle hamper this identification; this already happens in the above simple example, where the spectral footprint of the persistent modes erroneously suggests a six-fold permutation. Numerical effects enhance this identification in actual mapping matrices, though, by distorting the spectrum such that the permutation spectrum $\mathcal{P}(k)$ emerges closest to the unit circle (Section 4). This beneficial side effect of numerical errors has in fact already been exploited in Singh *et al.* [34].

3.6.2. Clusters of structures formed within/by chaotic seas

Clusters of structures associated with chaotic seas may emerge in two ways. First, in connection with multiple chaotic seas that are spatially-separated by e.g. symmetry planes. Second, in connection with clusters of higher-order hyperbolic points within one chaotic sea (Section 2.1). The block structure for the former kind identifies with that of island clusters, given by (21) and (23), upon substitution of $\mathbf{\Pi}_i$ by $\boldsymbol{D}_i$. The spectrum retains the form (24) in the simplified case of identical block matrices $\boldsymbol{D}$ and its typical footprint is demonstrated in Figure 7(b) for equal block matrices $\boldsymbol{D}$ following (15) and $k = 3$. Important difference with the island case is that here only the permutation spectrum $\mathcal{P}(k)$ emerges on the unit circle on account of but one eigenvalue $\lambda = 1$ for each $\boldsymbol{D}_i$ (Property 5).

The case of clusters of structures within one chaotic sea is fundamentally

different in that stringent spatial separation of individual elements of the cluster in disconnected groups of cells (as in an island chain) is absent. Manifold pairs of the periodic points each demarcate spatial areas $\mathcal{M}_i$ that, reminiscent of a jigsaw puzzle, interconnect and combined cover the chaotic sea by clustering following $\mathcal{M}_1 \cup \mathcal{M}_2 \cup \cdots \cup \mathcal{M}_k$. The highly-complex spatial structure of these conjugate regions and their intricate connections prohibit direct transformation into a block-diagonal structure similar to (21). Material nonetheless wanders cyclically through the chaotic sea via a directed cycle $\mathcal{M}_1 \rightarrow \mathcal{M}_2 \rightarrow \cdots \rightarrow \mathcal{M}_k$ in a manner akin to island chains (Section 3.6.1). This implies a similar permutation structure as (21) yet here "hidden" in the eigenmode decomposition of the block matrix $\boldsymbol{A}$ following

$$\boldsymbol{V}^{-1}\boldsymbol{A}\boldsymbol{V} = \begin{bmatrix} 1 & \mathbf{0} \\ \mathbf{0} & \boldsymbol{\Lambda} \end{bmatrix}, \quad \boldsymbol{\Lambda} = \boldsymbol{\Pi}_*\boldsymbol{\Lambda}_*, \quad \boldsymbol{\Lambda}_* = \begin{bmatrix} \boldsymbol{\Lambda}_1 & & \\ & \ddots & \\ & & \boldsymbol{\Lambda}_k \end{bmatrix}, \tag{25}$$

where factorisation into permutation and block-diagonal matrices occurs in eigenspace instead of in physical space. It must be stressed that the permutation acts only on the decaying modes, since only these modes contribute to the redistribution of material. The sole persistent mode, represent by the isolated unit entry in (25), corresponds to the trivial mode $\lambda = 1$ with homogeneous eigenvector covering the entire chaotic sea. Presuming, similar as before, identical $\boldsymbol{\Lambda}_1 = \boldsymbol{\Lambda}_2 = \cdots = \bar{\boldsymbol{\Lambda}}$ yields $eig(\boldsymbol{A}) = [1, \mathcal{P}(k) \times \mathcal{Q}]$, with here $\mathcal{Q} = eig(\bar{\boldsymbol{\Lambda}})$, as corresponding eigenvalue spectrum for $\boldsymbol{A}$. The typical spectral footprint of this kind of LCS is illustrated in Figure 7(c) for $\bar{\boldsymbol{\Lambda}} = diag(3/4, 1/2, -1/2)$; it deviates slightly from (24) by the presence of only eigenvalue $\lambda = 1$ on the unit circle. Compare this with the period-4 cluster of hyperbolic points for the TPSF at $T = 1.6$ in Singh *et al.* [34].

3.7. Implications for transport properties

The specific composition of the mapping matrix manifests itself in the transport properties. Presence of a block-diagonal structure implies disconnected flow regions, each corresponding with one block matrix, separated by KAM tori.

Conversely, absence of such a structure thus implies a system devoid of transport barriers. The most direct way to investigate this is via transformation (13). However, a generic algorithm is unavailable (Section 3.3). An indirect way exists in an eigenvalue decomposition. Eigenvalue $\lambda_{\max} \equiv \max_k |\lambda_k|$ of the non-trivial eigenmodes significantly smaller than unity implies one regular stochastic matrix (Property 5) and, in consequence, absence of a block-diagonal structure. Though efficient algorithms are available, this approach nonetheless is computationally intensive. A pragmatic alternative is to exploit the modal structure (10), which may be recast as

$$\boldsymbol{\Phi} = \boldsymbol{\Phi}_\infty + \Delta\boldsymbol{\Phi}, \quad \boldsymbol{\Phi}_\infty = \sum_{k\in\mathcal{K}_1} \lambda_k^{(1)} \boldsymbol{v}_k^{(1)} \boldsymbol{v}_k^{(1)}, \quad \Delta\boldsymbol{\Phi} = \sum_{k\in\mathcal{K}_2\cup\mathcal{K}_3} \lambda_k^{(2,3)} \boldsymbol{v}_k^{(2,3)} \boldsymbol{v}_k^{(2,3)}, \tag{26}$$

with $\boldsymbol{\Phi}_\infty = \lim_{p\to\infty} \boldsymbol{\Phi}^p$ and $\Delta\boldsymbol{\Phi}$ the asymptotic and transient contributions encompassing the persistent ($|\lambda_k^{(1)}| = 1$) and decaying ($|\lambda_k^{(2,3)}| < 1$) modes, respectively. (Hence $\lim_{p\to\infty} \Delta\boldsymbol{\Phi}^p = \mathbf{0}$.) The structure of the asymptotic contribution $\boldsymbol{\Phi}_\infty$ depends essentially on the presence/absence of transport barriers and may thus serve as a first indicator for a block-diagonal structure. Three kinds of asymptotic states $\boldsymbol{\Phi}_\infty$ may occur (Section 3.4): (i) inhomogeneous $\boldsymbol{\Phi}_\infty = \boldsymbol{L}$ (identical columns) in case $\boldsymbol{\Phi}$ is a regular stochastic matrix; (ii) homogeneous matrix $\boldsymbol{\Phi}_\infty = \boldsymbol{H}$ in case $\boldsymbol{\Phi}$ is a regular doubly-stochastic matrix; (iii) inhomogeneous periodic $\boldsymbol{\Phi}_\infty = \boldsymbol{\Phi}_\infty^k$ (non-identical columns) in case $\boldsymbol{\Phi}$ admits transformation into block-diagonal structure (13). The latter structure signifies disconnected flow regions and, inherently, presence of transport barriers. Important to note is that this affords a generic way to determine the global qualitative transport properties that, in contrast with e.g. Poincaré sectioning, is independent of the initial state.

The generic matrix properties also yield quantitative information on the transport properties. For the typical case of equidistant mapping grids, the block size in block-diagonal mapping matrices is a direct measure for the extent of the individual flow regions. This enables, once the nature of individual blocks (i.e. island or chaotic sea), has been established, evaluation of the relative area occupied by islands via $A_I = (N - S)/N$, where $0 \leq A_I \leq 1$. Here N and S

correspond with total number of cells and cells covering islands, respectively, which follow readily from the row/column-wise extents of the full matrix and the blocks. The homogenisation rate within both global and local chaotic seas directly relates to the corresponding $\lambda_{\max}$ through the characteristic time $\tau = -T/\ln|\lambda_{\max}|$ for the decay of inhomogeneous states [34].

4. The mapping matrix for non-conformal grids

Premise for attainment of the mapping composition examined in Section 3 is that the mapping grid is perfectly conformal with the transport barriers separating islands from chaotic seas (Section 2.2). However, intricate entities as island chains and cantori emanating from KAM tori (Section 2.1) render a fully conformal mapping grid impossible. Moreover, its creation, even if possible, is highly impractical, as it requires *a priori* detailed knowledge of the LCSs. Hence, typical mapping matrices rely on non-conformal grids.

The principal consequence of non-conformal mapping grids is that the modal structure (10) breaks down in favour of

$$\widetilde{\mathbf{\Phi}} = \sum_{k=1}^{N} \widetilde{\lambda}_k \widetilde{\boldsymbol{v}}_k \widetilde{\boldsymbol{v}}_k, \tag{27}$$

with $\widetilde{\mathbf{\Phi}}$ possessing the properties of a regular stochastic matrix (column sums still amount to unity). This means that the eigenmodes consist of one trivial eigenvalue $\widetilde{\lambda}_1 = 1$ and eigenvalues $|\widetilde{\lambda}_k| < 1$ for $k > 1$ (Property 5). Hence, the eigenvalue spectrum, save the trivial one, resides entirely within the unit circle under non-conformal conditions. Eigenvector $\widetilde{\boldsymbol{v}}_1$ is homogeneous only in case $\widetilde{\mathbf{\Phi}}$ is doubly-stochastic (i.e. $\widetilde{\mathbf{\Phi}} = \widetilde{\mathbf{\Xi}}$) (Property 1). In the particle-based approach this eigenvector may be inhomogeneous (Section 3.4). Other eigenvectors are always inhomogeneous and include those associated with either islands or seas, as illustrated in Figure 3, augmented by global eigenmodes covering both islands and seas. Figure 8(a) gives a typical global eigenmode for the TSPF at $T = 0.8$.

The diffusion-induced global eigenmodes represent material exchange between elliptic islands and chaotic seas and have significant non-zero contributions throughout the entire flow domain. Their spatial structure nonetheless

correlates well with said Lagrangian entities, as is evident upon comparing Figure 8(a) with the corresponding Poincaré section in Figure 1(b). This can be understood by realizing that these global eigenmodes are basically eigenmodes of adjacent LCSs "glued together" by the localized numerical diffusion near transport barriers induced by non-conformity of the mapping grid.

Mapping matrices for conformal and non-conformal grids formally relate via

$$\widetilde{\boldsymbol{\Phi}} = \boldsymbol{\Phi} + \boldsymbol{E} = \begin{bmatrix} \widetilde{\boldsymbol{\Phi}}_1 & \boldsymbol{E}_{1,2} & & \cdots & & \boldsymbol{E}_{1,k} \\ \boldsymbol{E}_{2,1} & \ddots & & & & \\ & & \widetilde{\boldsymbol{\Phi}}_i & \ddots & & \vdots \\ \vdots & & \ddots & \widetilde{\boldsymbol{\Phi}}_{i+1} & & \\ & & & & \ddots & \boldsymbol{E}_{k-1,k} \\ \boldsymbol{E}_{k,1} & & \cdots & & \boldsymbol{E}_{k,k-1} & \widetilde{\boldsymbol{\Phi}}_k \end{bmatrix}, \tag{28}$$

with $\boldsymbol{E} \equiv \widetilde{\boldsymbol{\Phi}} - \boldsymbol{\Phi}$ the difference matrix. Presence of the global eigenmodes in $\boldsymbol{E}$ prevents its transformation to a true block-diagonal structure (13). However, the "contaminated" mapping matrix $\widetilde{\boldsymbol{\Phi}}$ still is diagonally-dominant (i.e. $|\boldsymbol{E}| \ll |\widetilde{\boldsymbol{\Phi}}_i|$) yet with weak coupling between blocks. Inhomogeneity of $\widetilde{\boldsymbol{v}}_1$ reflects departures from solenoidality and has a comparable impact upon the mapping matrix as numerical diffusion (Section 2.2). Hence, it may serve as indicator for the typical departure $\epsilon = |\boldsymbol{E}|/|\boldsymbol{\Phi}|$, with $|.|$ some matrix norm, from conformal-grid conditions. Figures 8(b) and (c) give this mode for $N = 900$ and $N = 2500$, respectively, where the inhomogeneity $\Delta v = \max(\boldsymbol{v}_1) - \min(\boldsymbol{v}_1)$ in former and latter case amounts to $\Delta v \sim \mathcal{O}(10^{-2})$ and $\Delta v \sim \mathcal{O}(10^{-3})$. Through $|\boldsymbol{E}| \sim \mathcal{O}(\Delta v)$ and $|\boldsymbol{\Phi}| \sim \mathcal{O}(1)$ this yields $\epsilon \sim \mathcal{O}(10^{-2})$ and $\epsilon \sim \mathcal{O}(10^{-3})$ for $N = 900$ and $N = 2500$, respectively. This exposes rapid diminution of numerical diffusion due to non-conformity with increasing N. Note that the spatial correlation between $\widetilde{\boldsymbol{v}}_1$ and the associated transport barriers (Figure 1) substantiates the above assumption that this eigenmode is indicative of numerical diffusion.

An advantageous side effect of numerical diffusion is that it enhances discernibility of the spectral footprint of island clusters. Numerical diffusion means

that the island-wise permutation matrices $\mathbf{\Pi}_i$ in (21) deform into island-wise matrices that approximately define regular stochastic matrices $\boldsymbol{D}_i$ in the sense that column sums are close yet not identical to unity. (This property is retained only by the total matrix $\widetilde{\mathbf{\Phi}}$.) Spectrum eig($\widetilde{\mathbf{\Phi}}$), save the trivial mode, residing within the unit circle implies $|\lambda| < 1$ for $\lambda \in \text{eig}(\boldsymbol{D}_i)$. Presuming again island-wise identical matrices within a period-k island chain leads to an equivalent spectrum (24) of the associated block matrix yet with parent spectrum $\mathcal{Q}$ comprising eigenvalues with decreasing magnitude, i.e. $1 > |\lambda_1| > |\lambda_2| > \cdots > |\lambda_K|$. This causes contraction of the spectral footprint of the persistent eigenmodes (Figure 7(a)) onto concentric circles in a similar way as illustrated in Figure 7(b) for clusters of separated chaotic seas ($k = 3$), albeit with outer circle inside the unit circle. Here each concentric circle accommodates a rescaled version of the permutation spectrum $\mathcal{P}$, thus considerably enhancing its detection compared to the ideal case in Figure 7(a). This effect greatly benefits isolation of island clusters and has already been exploited by Singh *et al.* [34].

5. A representative example

The composition of the mapping matrix is demonstrated by way of the TPSF for $T = 0.56$. To this end the permutation matrix $\boldsymbol{P}$ in (13) is manually constructed by subdivision of the cells of the 50×50-cell mapping grid into groups covering different LCSs (Figure 1(a)). Here three (clusters of) LCSs can be discerned: two period-1 islands; encircling island chains; one chaotic sea. Further spatial features are of sub-cell scale and thus beyond the adopted mapping grid. The original mapping matrix $\mathbf{\Phi}$ is ordered according to cell position in the regular grid; numbering starts in the upper left corner (cell 1) and row-wise progresses downwards to the lower right corner (cell 2500). The permutation is visualized in Figure 9 by an overlay of the mapping grid and the Poincaré section, with cell groups corresponding with said Lagrangian entities highlighted in colour.

Figure 10 gives the original mapping matrix $\mathbf{\Phi}$ (panel (a)) and its permuted counterpart $\mathbf{\Phi}''$ according to (13) (panel (b)) in a 2D representation with ver-

tical/horizontal coordinates identifying with rows/columns. Markers and blank regions indicate non-zero and zero entries, respectively. Colour coding in $\boldsymbol{\Phi}''$ coincides with that of the cell groups in Figure 9; vertical and horizontal lines separate the cell groups. This discloses a symmetric matrix with a distinct band structure in $\boldsymbol{\Phi}$ comprising a diagonal band and two off-diagonal regions in upper-right and lower-left corners. The latter emanate from the periodic boundary conditions; the symmetry results from the time-reversal symmetry of the flow $\boldsymbol{F}$ (Section 2.1).

The permuted matrix $\boldsymbol{\Phi}''$ closely resembles a block diagonal structure, where block matrices correlate with the LCSs. The individual blocks exhibit weak coupling through the non-zero entries in the off-diagonal blocks due to numerical effects. This essentially confirms the composition of the mapping matrix predicted in Sections 3 and 4. Important to note is that the weak coupling primarily concerns the chaotic sea (green) and the period-1 islands (blue and cyan); the off-diagonal blocks adjacent to the diagonal blocks of the period-1 islands are completely devoid of non-zero entries, signifying complete decoupling. This is consistent with the fact that numerical effects are most prominent in the transition region between surviving (portions of) islands and the chaotic sea (Section 4). The blocks corresponding to period-1 islands and encircling island chains are, similar to these Lagrangian entities, of equal shape, which is a further manifestation of the beforementioned time-reversal symmetry of $\boldsymbol{F}$.

Reordering the block matrix $\boldsymbol{A}$ in $\boldsymbol{\Phi}''$ corresponding with the island chain highlighted in Figure 11(a) (indicated in red in Figures 9 and 10(b)) island-wise by their position within the chain (blue-cyan-black-red-green-magenta) exposes the intra-cluster structure of the mapping matrix. (The previous permutation orders cells within groups according to their row position in the original matrix.) Block matrix $\boldsymbol{A}$ thus reordered is given in Figure 11(b) and adopts the generic permutation form (21) for a period-6 cluster. Important to note here is that the individual blocks are of unequal size, disabling a matrix decomposition (23) and necessitating a tensor-based decomposition instead (Section 3.6.1). The invariance of the cluster as a whole dictates that $\boldsymbol{A}^k$, with here $k = 6$, collapses

on the generic block-diagonal structure following (22), where the sequence of blocks corresponds with the position of the islands in the cluster. Figure 11(c) shows the structure of $\boldsymbol{A}^k$, with colour coding as before, and visually verifies compliance with this essential condition.

The eigenvalue spectrum of $\boldsymbol{A}$ is given in Figure 12(a) and coincides well with the generic spectral footprint of island chains predicted in Section 3.6.1 in that it exhibits a distinct six-fold rotationally-symmetric pattern closely resembling the ideal form (24) for $k = 6$. Its confinement within a circle $\lambda_{\max} \equiv \max_k |\lambda_k|$ (dashed), with $\lambda_k \in \mathcal{Q}$ and $\lambda_{\max} = 0.9218$, is caused by the contraction of the spectrum of the persistent eigenmodes onto (approximately) concentric circles $|\lambda| < 1$ due to numerical effects (Section 4). This exposes a cluster of six eigenvalues, equidistantly distributed over the outer circle $\lambda_{\max}$ (indicated by circles in Figure 12(a)), as the permutation spectrum $\mathcal{P}(k)$. Hence, the actual spectral footprint is in excellent agreement with its predicted emergence. The significant departure from the unit circle signifies a relatively strong effect of numerical diffusion, which is a direct consequence of the comparably high cell-size to feature-size ratio in the island chain. Typical eigenvectors are given in Figures 12(b) $\lambda = \lambda_{\max}$ and (c) $\lambda = -\lambda_{\max}$ and, consistent with Conjecture 5, indeed reveal spatial distributions that combined cover the entire island chain.

Transformation into a block-diagonal structure has in the above been accomplished by way of a manually-constructed permutation matrix $\boldsymbol{P}$. For generic mapping matrices this can formally be achieved through transformation (13), which is far from trivial, however. Determination of whether a block-diagonal structure is present may adopt the approach based on the asymptotic mapping matrix $\boldsymbol{\Phi}_\infty = \lim_{p\to\infty} \boldsymbol{\Phi}^p$ proposed in Section 3.7. Here it must be taken into account that numerical effects cause block matrices of islands to (approximately) become regular stochastic matrices yet with eigenvalues significantly closer to the unit circle than for chaotic seas (Section 4). Hence, block matrices corresponding with islands strictly spoken no longer converge on inhomogeneous periodic matrices $\boldsymbol{\Phi}_\infty = \boldsymbol{\Phi}_\infty^k$ yet nonetheless closely follow that scenario in

that their progression towards a homogeneous asymptotic state is considerably slower than that of block matrices associated with chaotic seas. This implies relatively long-lived inhomogeneities in the mapping matrix in cell groups coinciding with islands during its evolution towards $\boldsymbol{\Phi}_\infty = \boldsymbol{L}$ (regular stochastic matrix) or $\boldsymbol{\Phi}_\infty = \boldsymbol{H}$ (regular doubly-stochastic matrix) in a manner reminiscent of strange eigenmodes in evolving scalar fields [34]. Numerical investigation confirms this behaviour and reveals that the mapping matrix within 10-15 periods converges on an asymptotic state with columns coinciding within $\mathcal{O}(10^{-14})$. Figure 13 gives the spatial distribution of those columns for T as indicated and exposes an evident dependence on the Lagrangian flow structure (Figure 1). Case $T = 0.56$ adopts a pattern that closely correlates with the period-1 islands; case $T = 1.6$, in contrast, assumes a random distribution, consistent with its globally-chaotic state. Important to note is that both states correspond with the inhomogeneous asymptotic matrix $\boldsymbol{\Phi}_\infty = \boldsymbol{L}$, with fluctuations of $\mathcal{O}(10^{-4})$, on account of the fact that $\boldsymbol{\Phi}$ is a regular stochastic matrix. Thus the departure from a true doubly-stochastic mapping matrix $\boldsymbol{\Xi}$ (Section 2.2) in fact is beneficial here in that it facilitates robust detection of inhomogeneities that, in turn, imply transport barriers and, inherently, an approximate block-diagonal structure of the mapping matrix according to (28).

6. Conclusions

The present study investigates the composition of the mapping matrix in relation to the Lagrangian flow structure and expands on earlier work by Singh *et al.* [34]. This is motivated by finding ways to systematically manipulate the properties of the mapping matrix for various transport purposes. Primary objective is achievement of efficient mixing, but other aims as accomplishment of distinct concentration distributions or Lagrangian flow structures for e.g. (local) catalysation of chemical reactions in labs-on-a-chip or manufacturing of anisotropic micro-fibres, become increasingly relevant with the growing role of micro-fluidics. Redistribution of material by the mapping matrix is essentially the same as flows in networks and thus admits representation by graphs and

associated distribution matrices. This facilitates a robust analysis on the generic composition of the mapping matrix – and its underlying continuous transport operator – that combines concepts and results from operator, graph and matrix theory.

The mapping matrix possesses a block-diagonal structure that reflects the formation of distinct – and spatially disconnected – Lagrangian coherent structures (LCSs) in the flow field: elliptic islands and chaotic seas. Each block matrix represents one such LCS and defines a mapping matrix in its own right. The latter, in turn, identify with stochastic matrices, which implies a composition based on two elementary matrices, i.e. permutation matrices and regular stochastic matrices, that directly relate to the dynamics. Permutation matrices represent purely advective redistribution of material; regular stochastic matrices represent the (local) homogenisation of concentration distributions due to the interplay of advection and weak, yet physically inevitable, molecular diffusion. Hence, permutation matrices are inextricably linked with asymptotic (inhomogeneous) concentration distributions – and thus persistent eigenmodes – as well as with periodic events (e.g. cyclic redistribution of material in island chains). Regular stochastic matrices correspond with transient states and, inherently, with decaying eigenmodes. Each LCS leaves a particular spectral footprint in the eigenvalue spectrum of the mapping matrix that betrays its kind and its periodicity. The present study thus exposed the fundamental connection between the Lagrangian flow structure and the spectral properties of the (discrete) transport operator.

The matrix structure has been investigated for a representative example accommodating a typical Lagrangian flow structure comprising islands of various periodicity embedded in a chaotic sea. This yields a mapping matrix that is entirely consistent with the predicted composition on the basis of the corresponding LCSs. A block-diagonal structure, implying transport barriers and disconnected LCSs, is found with block matrices according to the spectral footprints of the associated LCSs. Non-conformity of the mapping grid with transport barriers introduces a weak coupling between the block matrices through

small off-diagonal contributions. This alters the spectral footprints of the LCSs by shifting the eigenvalues slightly inside the unit circle yet with retention of their characteristic structure.

The fundamental connection between the mapping matrix and generic flows in networks may facilitate development of control strategies for the accomplishment of specific transport properties and Lagrangian flow structures. This may have particular potential in micro-fluidic applications due to the various promising flow-forcing methods [24, 25, 27]. The impact and scope of flow control on the basis of the Lagrangian flow structure may be augmented by further unravelling its connection with the composition of the mapping matrix. Efforts to this effect are in progress. Extension to essentially 3D flows is, owing to its far more more complex Lagrangian flow structure [49–53], likely to offer many new ways for accomplishing transport capabilities. However, this is a formidable challenge, since truly 3D transport phenomena remain elusive to date [54].

References

[1] N. Harnby, M. Edwards, A. Nienow, Mixing in the Process Industries, Butterworth-Heinemann, Oxford, 1997.

[2] R. Thakur, C. Vial, K. Nigam, E. Nauman, G. Djelveh, Static mixers in the process industries – a review, Trans IChemE 81 (2003) 787.

[3] J. M. Ottino, Mixing, chaotic advection and turbulence, Annual Review of Fluid Mechanics 22 (1990) 207–253.

[4] S. Wiggins, The dynamical systems approach to lagrangian transport in oceanic flows, Annu. Rev. Fluid. Mech. 37 (2004) 295–328.

[5] P. van Keken, E. Hauri, C. Ballentine, Mantle mixing: the generation, preservation, and destruction of chemical heterogeneity, Annu. Rev. Earth Planet Sci. 20 (2002) 493–525.

[6] H. Aref, Stirring by chaotic advection, J. Fluid Mech. 143 (1984) 1–21.

[7] J. M. Ottino, The kinematics of mixing: Stretching, Chaos, and Transport, Cambridge University Press, Cambridge, 1989.

[8] H. Aref, The development of chaotic advection, Phys. Fluids 14 (4) (2002) 1315–1325.

[9] R. Weinekötter, Compact and efficient continuous mixing processes for production of food and pharmaceutical powders, Trends Food Sci. Tech. 20 (2009) S48.

[10] B. Weigl, G. Domingo, P. Labarre, J. Gerlach, Towards non- and minimally instrumented, microfluidics-based diagnostic devices, Lab Chip 8 (2008) 1999.

[11] T. LaPorte, C. Wang, Continuous processes for the production of pharmaceutical intermediates and active pharmaceutical ingredients, Curr. Opin. Drug Discov. Devel. 10 (2007) 738.

[12] S. Becht, R. Franke, A. G. elmann, H. Hahn, Micro process technology as a means of process intensification, Chem. Eng. Technol. 30 (2007) 295.

[13] H. A. Stone, A. D. Stroock, A. Ajdari, Engineering flows in small devices: Microfluidics toward a lab-on-a-chip, Annu. Rev. Fluid Mech. 36 (2004) 381–411.

[14] J. M. Ottino, S. Wiggins, Introduction: mixing in microfluidics, Phil. Trans. R. Soc. London A 362 (2004) 923–935.

[15] C. Hansen, S. Quake, Microfluidics in structural biology: smaller, faster ... better, Curr. Opin. Struct. Biology 13 (2002) 538.

[16] D. Beebe, G. Mensing, G. Walker, Physics and applications of microfluidics in biology, Annu. Rev. Biomed. Engng 4 (2002) 261.

[17] S. Wiggins, J. M. Ottino, Foundations of chaotic mixing, Phil. Trans. R. Soc. London A 362 (2004) 937–970.

[18] M. Branicki, S. Wiggins, An adaptive method for computing invariant manifolds in non-autonomous, three-dimensional dynamical systems, Physica D 238 (2009) 1625–1657.

[19] I. Mezić, S. Wiggins, A method for visualization of invariant sets of dynamical systems based on ergodic partition, Chaos 9 (1999) 213–218.

[20] I. Mezić, F. Sotiropoulos, Ergodic theory and experimental visualization of chaos, Phys. Fluids 14 (2002) 2235–2243.

[21] G. Metcalfe, M. Speetjens, D. Lester, H. Clercx, Beyond passive: chaotic transport in stirred fluids, Adv. Appl. Mech. 45 (2011) 109–188.

[22] S. Cerbelli, A. Adrover, F. Creta, M. Giona, Foundations of laminar chaotic mixing and spectral theory of linear operators, Chem. Eng. Sci. 61 (2006) 2754–2761.

[23] W. Liu, G. Haller, Strange eigenmodes and decay of variance in the mixing of diffusive tracers, Physica D 188 (2004) 1–39.

[24] T. G. Kang, M. A. Hulsen, P. D. Anderson, J. M. J. den Toonder, H. E. H. Meijer, Chaotic mixing induced by a magnetic chain in a rotating magnetic field, Phys. Rev. E 76 (2007) 066303.

[25] J. M. J. den Toonder, F. M. Bos, D. J. Broer, L. Filippini, M. Gillies, J. de Goede, T. Mol, M. A. Reijme, W. Talen, P. D. A. H. Wilderbeek, V. Khatavkar, Artificial cilia for active micro-fluidic mixing, Lab Chip 8 (2008) 533–541.

[26] T. Squires, Induced charge electrokinetics: fundamental challenges and opportunities, Lab Chip 9 (2009) 2477.

[27] M. F. M. Speetjens, H. N. L. de Wispelaere, A. A. van Steenhoven, Multifunctional lagrangian flow structures in 3d aceo micro-flows, Fluid. Dyn. Res 43 (2011) 035503.

[28] I. Mezić, Spectral properties of dynamical systems, model reduction and decompositions, Nonlin. Dyn. 41 (2005) 309–325.

[29] C. Rowley, I. Mezić, S. Bagheri, P. Schlatter, D. Henningson, Spectral analysis of nonlinear flows, J. Fluid Mech. 614 (2009) 115–127.

[30] P. D. Anderson, O. S. Galaktionov, G. W. M. Peters, H. E. H. Meijer, C. L. Tucker, Material stretching in laminar mixing flows: extended mapping technique applied to the journal bearing flow, Int. J. Numer. Methods Fluids 40 (2002) 189–196.

[31] M. K. Singh, P. D. Anderson, M. F. M. Speetjens, H. E. H. Meijer, Optimizing the Rotated Arc Mixer, AIChE J. 54 (2008) 2809–2822.

[32] Y. L. Guer, E. Schall, A mapping tool using anisotropic unstructured meshes to study mixing in periodic flows, Chem Eng Sci 59 (7) (2004) 1459–1472.

[33] O. S. Galaktionov, P. D. Anderson, G. W. M. Peters, H. E. H. Meijer, Mapping approach for 3d laminar mixing simulation: application to industrial flows, Int. J. Numer. Methods Fluids 40 (1-2) (2002) 189–196.

[34] M. K. Singh, M. F. M. Speetjens, P. D. Anderson, Eigenmode analysis of scalar transport in distributive mixing, Phys. Fluids 21 (2009) 093601.

[35] S. Cerbelli, A. Adrover, M. Giona, Enhanced diffusion regimes in bounded chaotic flows, Physics Letters A 312 (2003) 355–362.

[36] S. Cerbelli, V. Vitacolonna, A. Adrover, M. Giona, Eigenvalue-eigenfunction analysis of infinitely fast reactions and micromixing regimes in regular and chaotic bounded flows, Chem. Eng. Sci. 59 (2004) 2125–2144.

[37] O. Gorodetskyi, M. Giona, P. D. Anderson, Exploiting numerical diffusion to study transport and chaotic mixing for extremely large péclet values, Europhys. Lett. 97 (2012) 14002.

[38] E. Ott, Chaos in Dynamical Systems, Cambridge University Press, Cambridge, 2002.

[39] R. S. MacKay, J. D. Meiss, I. C. Percival, Stochasticity and transport in hamiltonian systems, Phys. Rev. Lett. 52 (1990) 697.

[40] Y.-C. Lai, T. Tél, Transient chaos: Complex Dynamics on Finite Time Scales, Springer, New York, 2011.

[41] V. V. Meleshko, G. W. M. Peters, Periodic points for two-dimensional stokes flow in a rectangular cavity, Physics Letters A 216 (1996) 87–96.

[42] M. F. M. Speetjens, H. J. H. Clercx, G. J. F. van Heijst, A numerical and experimental study on advection in three-dimensional stokes flows., J. Fluid Mech. 514 (2004) 77.

[43] R. Spencer, R. Wiley, The mixing of very viscous liquids, Journal of Colloid Science 6 (1951) 133–145.

[44] M. K. Singh, O. S. Galaktionov, H. E. H. Meijer, P. D. Anderson, A simplified approach to compute distribution matrices for the mapping method, Computers Chem. Engng 33 (2009) 1354–1362.

[45] S. H. Friedberg, A. J. Insel, L. E. Spence, Linear Algebra, Prentice Hall., New Jersey, 1997.

[46] G. Strang, Linear Algebra and its Applications, Harcourt Brace Jovanovich, San Diego, 1976.

[47] C. R. Paul, Fundamentals of Electric Circuit Analysis, Wiley, Chichester, 2001.

[48] F. Gebali, Analysis of Computer and Communication Networks, Springer, New York, 2008.

[49] I. Mezić, S. Wiggins, On the integrability and perturbation of three-dimensional fluid flows with symmetry, J. Nonlinear Sci. 4 (1994) 157–194.

[50] J. H. E. Cartwright, M. Feingold, O. Piro, Chaotic advection in three-dimensional unsteady incompressible laminar flow, J. Fluid Mech. 316 (1996) 259–284.

[51] M. F. M. Speetjens, H. J. H. Clercx, G. J. F. van Heijst, Inertia-induced coherent structures in a time-periodic viscous mixing flow, Phys. Fluids 18 (2006) 083603.

[52] I. Mezić, Break-up of invariant surfaces in actionangleangle maps and flows, Physica D 154 (2001) 51.

[53] G. Haller, Distinguished material surfaces and coherent structures in three-dimensional fluid flows, Physica D 149 (2001) 248277.

[54] S. Wiggins, Coherent structures and chaotic advection in three dimensions, J. Fluid Mech. 654 (2010) 1–4.

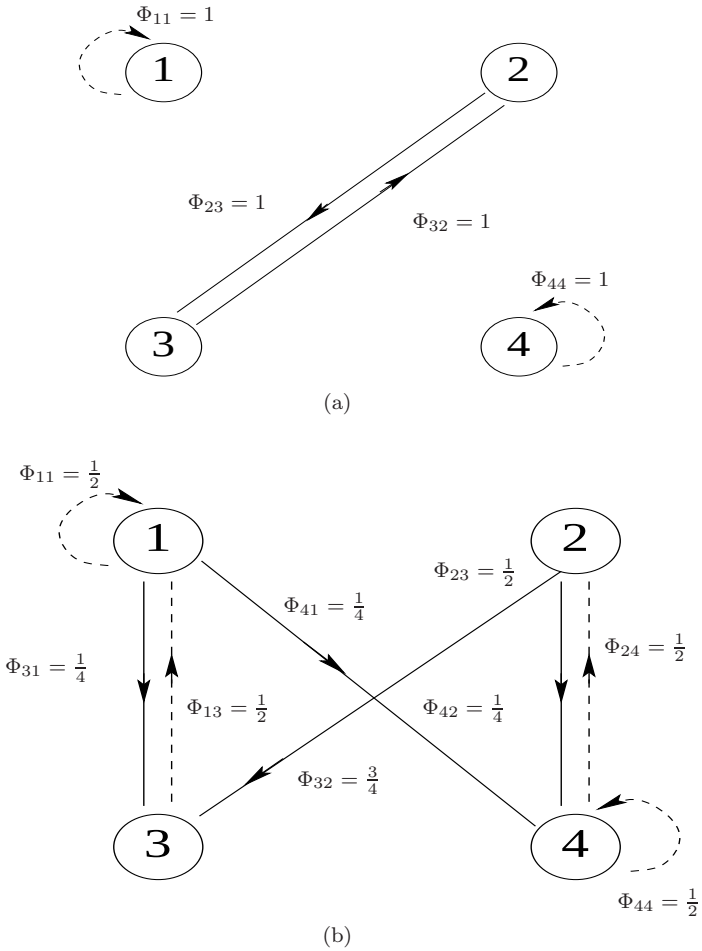

Figure 5: Transport by the elementary matrices: (a) permutation matrix $\mathbf{\Pi}$; (b) regular stochastic matrices $\boldsymbol{D}$. Shown graphs correspond to examples (15).

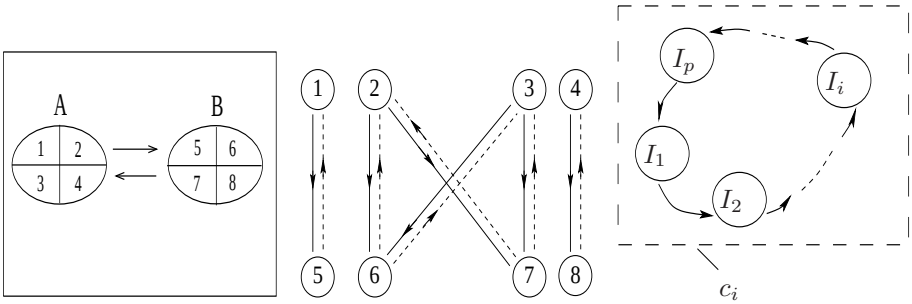

(a) (b) (c)

Figure 6: Transport within/between period-2 islands: (a) mapping grid; (b) graph for $\mathbf{\Pi}_A = \mathbf{\Pi}_B = \mathbf{\Pi}$ following (15); (c) inter-island permutation.

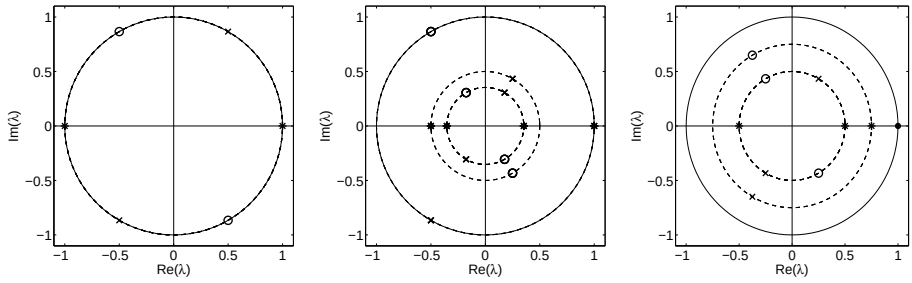

(a) (b) (c)

Figure 7: Spectral footprints of different types of Lagrangian coherent structures exemplified for periodicity $k = 3$: (a) a cluster of islands; (b) a cluster of chaotic seas; (c) clusters within one chaotic sea. Stars indicate the parent spectrum $\mathcal{Q}$; circles and crosses indicate permutations by ω and ω^2, respectively. The star-circle-cross sequence starting from $\lambda = 1$ coincides with the permutation spectrum $\mathcal{P}(k)$. The isolated eigenvalue $\lambda = 1$ (heavy dot) in panel (c) represents the trivial homogeneous eigenvector emanating from mass conservation.

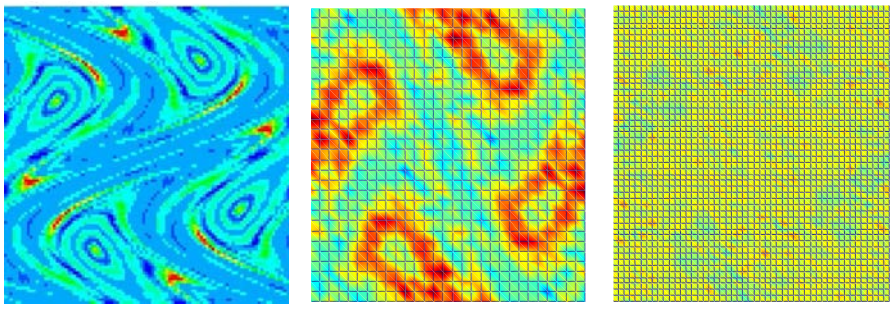

(a) (b) (c)

Figure 8: Effect of non-conformity of the mapping grid demonstrated for the TPSF at $T = 0.8$: (a) typical global eigenmode; (b) inhomogeneity of eigenmode $\widetilde{\boldsymbol{v}}_1$ for $N = 900$; (c) inhomogeneity of eigenmode $\widetilde{\boldsymbol{v}}_1$ for $N = 2500$. These inhomogeneities serve as indicator for numerical diffusion due to non-conformity. Red/blue indicate maximum/minimum magnitudes about zero level (green).

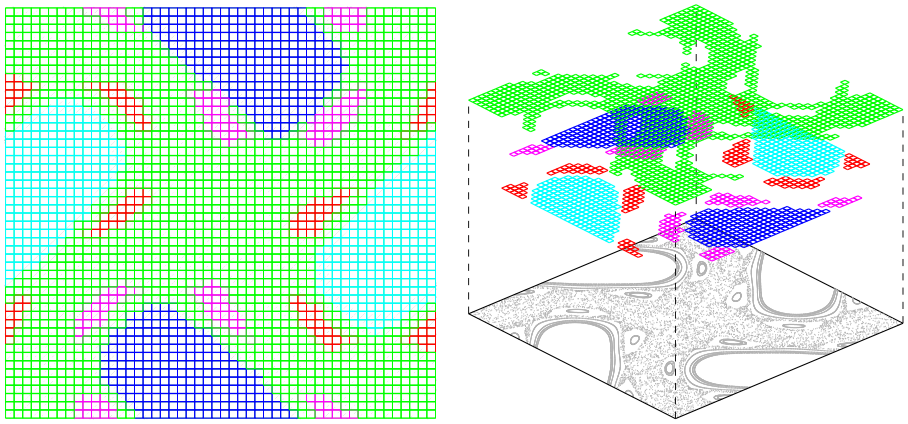

(a) (b)

Figure 9: Subdivision of the mapping grid according to transport barriers separating LCSs for the TPSF at $T = 0.56$: (a) planar view; (b) exploded view including Poincaré section. Colours distinguish different (clusters of) islands and chaotic regions.

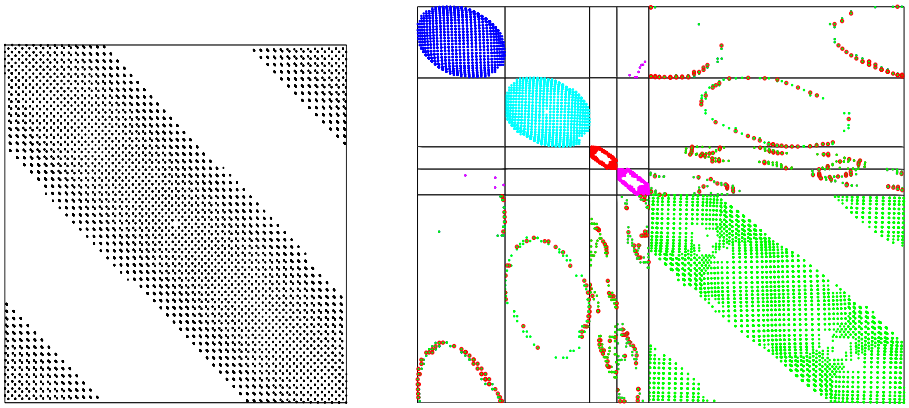

(a) (b)

Figure 10: Block-diagonal structure associated with disconnected LCSs for the TPSF at $T = 0.56$: (a) original matrix $\mathbf{\Phi}$ based on standard sequential cell numbering; (b) permuted matrix $\mathbf{\Phi}''$ using the subdivision of following Figure 9. Colours correspond with the LCSs in Figure 9.

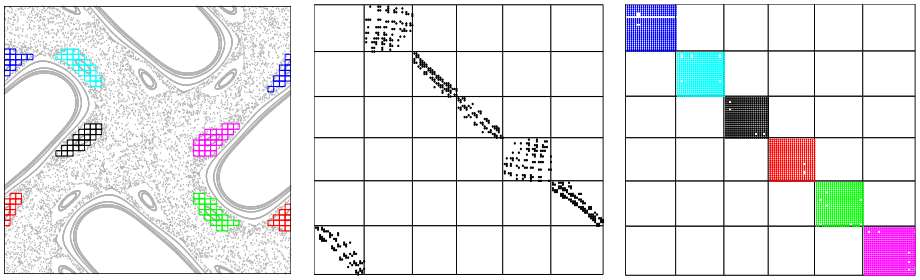

(a) (b) (c)

Figure 11: Composition of the block matrix $\boldsymbol{A}$ associated with a period-6 island chain of the TPSF at $T = 0.56$: (a) island chain with its 6 individual islands highlighted; (b) structure of $\boldsymbol{A}$; (c) diagonal structure of $\boldsymbol{A}^k$ ($k = 6$) reflecting the permutation along the individual islands.

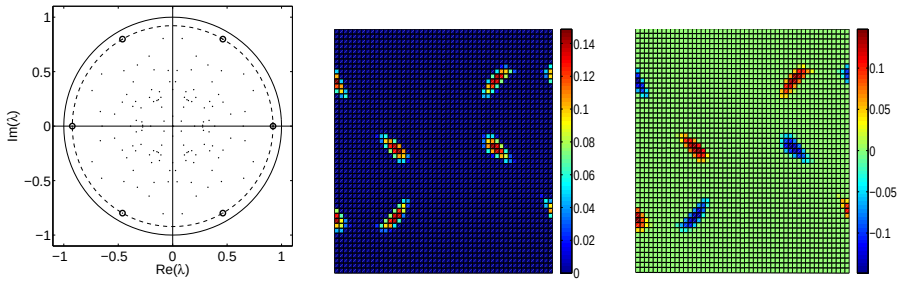

(a) (b) (c)

Figure 12: Footprint of the period-6 island chain for the TPSF at $T = 0.56$: (a) eigenvalue spectrum with the island chain located on the circle $|\lambda| = \lambda_{\max} = 0.9218$ (dashed) indicated by small circles; (b) eigenvector corresponding with $\lambda = \lambda_{\max}$; (c) eigenvector corresponding with $\lambda = -\lambda_{\max}$.

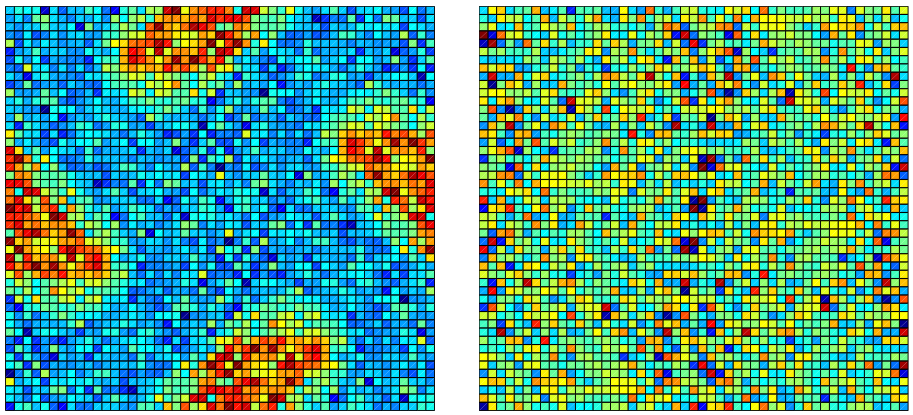

(a) (b)

Figure 13: Spatial pattern of the asymptotic mapping matrix $\mathbf{\Phi}_\infty$ for the TPSF and its correlation with the Poincaré map: (a) $T = 0.56$; (b) $T = 1.6$.